Structure of an open K_{ATP} channel reveals tandem PIP_2 binding sites mediating the Kir6.2 and SUR1 regulatory interface

Camden M. Driggers*, Yi-Ying Kuo, Phillip Zhu, Assmaa ElSheikh, and Show-Ling Shyng*

Department of Chemical Physiology and Biochemistry, School of Medicine, Oregon Health and Science University, Portland, OR 97239

*To whom correspondence may be addressed: Camden M. Driggers, driggerc@ohsu.edu; Show-Ling Shyng, shyngs@ohsu.edu

Key words: ATP-sensitive potassium channel, cryoEM structure, inward rectifier potassium channel, sulfonylurea receptor, ABC transporter, gating, phospholipid, PIP_2

Abbreviations: K_{ATP}, ATP-sensitive potassium channel; Kir, inward-rectifying potassium channel; SUR1, sulfonylurea receptor1; CTD, cytoplasmic domain of Kir6.2; KNtp, Kir6.2 N-terminal peptide; TMD, transmembrane domain; NBD, nucleotide binding domain of SUR1; ECL, extracellular loop; ICL, intracellular loop; βA, first part of β-sheet of CTD; M1 or M2, membrane helix 1 or 2 of Kir6.2; cryoEM, cryo-electron microscopy; TM, transmembrane; PIP_2, phosphatidylinositol 4,5-bisphosphate; ATP, adenosine triphosphate.

Abstract

ATP-sensitive potassium (K_{ATP}) channels, composed of four pore-lining Kir6.2 subunits and four regulatory sulfonylurea receptor 1 (SUR1) subunits, control insulin secretion in pancreatic β-cells. K_{ATP} channel opening is stimulated by PIP_2 and inhibited by ATP. Mutations that increase channel opening by PIP_2 reduce ATP inhibition and cause neonatal diabetes. Although considerable evidence has indicated PIP_2 in K_{ATP} channel function, previously solved open-channel structures have lacked bound PIP_2, and mechanisms by which PIP_2 regulates K_{ATP} channels remain unresolved. Here, we report cryoEM structure of a K_{ATP} channel harboring the neonatal diabetes mutation Kir6.2-Q52R, bound to PIP_2 in open conformation. The structure reveals two adjacent PIP_2 molecules between SUR1 and Kir6.2. The first PIP_2 binding site is conserved among PIP_2-gated Kir channels. The second site forms uniquely in K_{ATP} at the interface of Kir6.2 and SUR1. Functional studies demonstrate both binding sites determine channel activity. Kir6.2 pore opening is associated with a twist of the Kir6.2 cytoplasmic domain and a rotation of the N-terminal transmembrane domain of SUR1, which widens the inhibitory ATP binding pocket to disfavor ATP binding. The open conformation is particularly stabilized by the Kir6.2-Q52R residue through cation-π bonding with SUR1-W51. Together, these results uncover the cooperation between SUR1 and Kir6.2 in PIP_2 binding and gating, explain the antagonistic regulation of K_{ATP} channels by PIP_2 and ATP, and provide the mechanism by which Kir6.2-Q52R stabilizes an open channel to cause neonatal diabetes.

Introduction

The K_{ATP} channel expressed in pancreatic islet β-cells is a principal homeostatic regulator of insulin secretion [1-3]. Composed of four pore-forming Kir6.2 and four regulatory sulfonylurea receptor 1 (SUR1) subunits [4, 5], K_{ATP} channels determine the resting membrane potential, thus action potential firing, Ca^{2+} entry, and insulin secretion. The activity of K_{ATP} channels is

dynamically regulated by glucose changes via intracellular ATP and MgADP, which bind to inhibitory and stimulatory sites to close and open the channel, respectively [6, 7]. This enables insulin secretion to follow fluctuations in glucose concentrations. The central role of K_{ATP} channels in insulin secretion and glucose homeostasis is underscored by dysregulated insulin secretion and blood glucose in humans bearing K_{ATP} mutations: loss-of-function mutations cause congenital hyperinsulinism characterized by persistent insulin secretion despite life-threatening hypoglycemia [8, 9]; conversely, gain-of-function channel mutations result in neonatal diabetes due to insufficient insulin secretion [10].

In addition to adenine nucleotides-dependent regulation, membrane phosphoinositides participate in the gating activation of K_{ATP} channels [11, 12], as they do all other eukaryotic Kir channels [13]. PI(4,5)P_2 (denoted as PIP_2 unless specified) is the most abundant phosphoinositide in the plasma membrane [14]. Increasing PIP_2 levels increases the open probability (P_o) of K_{ATP} channels, whereas scavenging membrane PIP_2 with poly-lysine decreases channel P_o [11, 12]. Because increasing channel P_o by PIP_2 also decreases channel sensitivity to ATP inhibition [11, 12], a joint regulatory mechanism involving allosteric or binding competition between the two ligands has seemed likely [15]. In particular, the effect of PIP_2 on K_{ATP} channels has been assumed to derive from a putative conserved binding site in Kir6.2 having a position similar to the PIP_2 previously identified in crystal and cryoEM structures of homologous Kir2 and Kir3 [16-19]. Uniquely however, gating of Kir6.2 by PIP_2 is strongly modulated by its regulatory subunit SUR1. Compared to the fully assembled K_{ATP} channels, Kir6.2 channels lacking SUR1 partners display more than 10-fold lower P_o [11, 15, 20], which reflects reduced PIP_2 binding or gating, and are less sensitive to PIP_2 stimulation [11, 15]. Of particular interest, the SUR1 N-terminal transmembrane domain, TMD0, which interfaces with Kir6.2 [21-23], is sufficient to confer the high P_o of WT channels [24, 25], implicating a crucial role of SUR1-TMD0 in controlling Kir6.2 response to PIP_2.

To date, cryoEM structures of K_{ATP} channels determined for a variety of liganded and mutational states have yielded a structural spectrum encompassing open, closed, and inactivated conformations (reviewed in [6, 7, 26]). Careful comparisons have suggested mechanisms by which channel activity is regulated by the SUR subunit and nucleotides. However, confusion has grown regarding PIP_2 binding and gating. Two recently reported open- and pre-open mutant K_{ATP} channel cryoEM structures lack discernible PIP_2 at the putative binding site [27, 28]. Furthermore, purified wild-type (WT) K_{ATP} channels reconstituted in lipid bilayers lacking PIP_2 showed single channel openings [27]. These reports suggest that PIP_2 binding may be inessential for open channel transition [27]. Thus, notwithstanding robust data indicating PIP_2 involvement in physiological channel activation [11, 29, 30], how PIP_2 binds and modulates K_{ATP} channels remains enigmatic.

Our approach to understanding K_{ATP} channel activation and PIP_2 binding involved determining the structure of a K_{ATP} channel variant containing the neonatal diabetes-causing mutation Q52R in Kir6.2 [31, 32]. Kir6.2-Q52R markedly increases channel P_o and decreases the IC_{50} of ATP inhibition ~20-fold [31, 32]. Higher P_o could result from enhanced PIP_2 binding or its effect on gating. Intriguingly, the effect of this mutation on channel gating is SUR1-dependent; Kir6.2 channels containing the Q52R mutation but lacking the SUR1 subunit exhibit the same P_o and ATP sensitivity as Kir6.2 channels alone without the mutation [33]. The SUR1-dependent overactivity imparted by the Kir6.2 Q52R mutation indicated the possibility to probe the regulatory interaction between SUR1 and membrane PIP_2 on Kir6.2 gating.

Here, we present the cryoEM structure of the K_{ATP} channel harboring the neonatal diabetes Q52R mutation (denoted SUR1/Kir6.2$^{\mathbf{Q52R}}$ hereinafter) bound to PIP_2 in an open conformation. Surprisingly, two PIP_2 molecules bind in tandem in the open channel at the interface between Kir6.2 and SUR1. A first PIP_2 molecule binds within the site that is conserved among Kir

channels. A second PIP_2 molecule binds at an adjacent position, stacked within the regulatory interface between Kir6.2 and SUR1 TMDs. The open channel conformation is further stabilized by direct interaction between Q52R of Kir6.2 and SUR1-W51 located in TMD0. Accounting for decades of evidence from functional perturbation studies, the PIP_2-bound SUR1/Kir6.2^{Q52R} K_{ATP} structure unveils the agonist binding of PIP_2 in K_{ATP} channels, revealing that in addition to the ancestral Kir PIP_2 site, the incorporation of the regulatory SUR1 subunit creates a second regulatory PIP_2 binding site. The results implicate a novel mechanism through which SUR1, by cooperating with Kir6.2 for PIP_2 binding, stabilizes the K_{ATP} channel in an open state to control activity, and illuminate the molecular mechanism by which a human activating mutation in the K_{ATP} channel causes neonatal diabetes.

Results

Structure of an open SUR1/Kir6.2^{Q52R} K_{ATP} channel bound to PIP_2

To purify the neonatal diabetes variant SUR1/Kir6.2^{Q52R} K_{ATP} channel, we co-expressed Kir6.2^{Q52R} and SUR1 as independent polypeptides by transducing adherent mammalian COSm6 cells with recombinant adenovirus packaged with genes for rat Kir6.2^{Q52R} and FLAG-tagged hamster SUR1 (see Methods). To facilitate the capture of PIP_2-bound channel structure, we prepared a membrane fraction of COSm6 cells expressing the mutant channel, and enriched the native membranes with brain PIP_2, primarily containing 18:0/20:4 PI(4,5)P_2 (Avanti Polar Lipids), before detergent solubilization. We anticipated that addition of long-chain PIP_2 prior to detergent extraction would stably incorporate PIP_2 resistant to washout in subsequent purification steps. K_{ATP} channels were purified via the FLAG-tag on SUR1 and spotted on graphene oxide (GO)-coated grids for cryoEM (see methods). To maximize channels in PIP_2-bound open conformations, no ATP or ADP were added to the sample.

CryoEM micrographs showed mostly full SUR1/Kir6.2^{Q52R} K_{ATP} channel particles (Fig. S1). 2D classes indicate an ordered Kir6.2 and SUR1-TMD0, with a relatively more blurred SUR1-ABC core especially the nucleotide binding domains (NBDs) (Fig. S1). A non-uniform refinement with C4 symmetry using all good particles from 2D classification (71,075) in cryoSPARC resulted in an un-masked reconstruction of the full channel at 3.9 Å using the gold-standard Fourier shell correlation (GSFSC) cutoff of 0.143 (see Methods). The electron potential map shows relatively weak signal for TMD2 and NBD2 of SUR1 (Figs. S1, S2), indicating higher mobility of these domains. Multiple rounds of *ab initio* reconstruction without symmetry imposed (Figs. S1, S2) yielded a best 3D class containing 14,115 particles, which following a C4 non-uniform refinement in cryoSPARC with auto-masking that excluded SUR1-NBD2 resulted in a final map reconstruction of 2.9 Å by GSFSC within the autoFSC mask, or 3.3 Å resolution by GSFSC within a mask that includes the full K_{ATP} channel, that was used for model building (Figs.1, S2, Table S1). The full channel map shows a highly ordered Kir6.2 tetramer core and SUR1-TMD0 with local resolutions < 2.9 Å (Fig. S2). More particularly, the map revealed bound PIP_2 at the regulatory interface of Kir6.2 and SUR1 and an open Kir6.2 pore (Fig. 1) [34-36], and molecular rearrangements at the SUR1-Kir6.2 interface critical to gating, as we describe in detail in the following sections.

Tandem PIP_2 binding at the interface of Kir6.2 and SUR1

The cryoEM map, derived from SUR1/Kir6.2^{Q52R} K_{ATP} channels pre-incubated with exogenous brain PIP_2, showed density corresponding to two adjacent PIP_2 molecules occupying sites in a large pocket at the Kir6.2-SUR1 interface near the inner leaflet of the membrane bilayer (Figs. 2A, S3). The first PIP_2 occupies the predicted PIP_2 binding site of Kir6.2 based on comparisons with the homologous structures of Kir channels Kir2 and Kir3/GIRK bound to PIP_2 [16-19]. The second PIP_2 binding site, which is occupied by a PIP_2 with stronger map features than the first PIP_2 (Fig. S3), is nestled between SUR1 and the first PIP_2 binding site and in contact with both

Kir6.2 and SUR1 subunits (Fig. 2A-C). Both PIP_2 molecules were fit into the map by modelling as 18:0, 20:4 PI(4,5)P_2 (Figs.1B, 2B, 2C, S3A, S3B), which is the dominant form present in brain PIP_2 (~75%) [37], and both PIP_2 sites have map features for the phospho-head groups as well as long acyl chains that can be fit by a 18:0/20:4 PI(4,5)P_2 structure (monomer ID PT5) (Figs. 2B, 2C, S3B). Three other well-resolved lipid map features at the inner leaflet of the membrane bilayer were bound between SUR1-TMD0 and SUR1-TMD1 (Fig.S3A, C). These were best modeled by the common native phospholipids phosphatidylethanolamine and phosphatidylserine (Fig.S3B, D). The comparative fit of the different lipid species demonstrates that they can be distinguished using the reconstructed cryoEM maps (Fig. S3).

Structural analysis surrounding the PIP_2 head groups

The head group of the first PIP_2 at the ancestral binding site forms extensive polar interactions with surrounding residues (Fig. 2B, C). The phosphate groups are coordinated directly by Kir6.2 residues R176 and K67 while Kir6.2-W68 forms close interaction with the inositol ring, although K170, which is about 4.5 Å away and H175, which is about 5.5 Å away, are also in close proximity. Most of the head group-interacting residues are conserved in Kir2 and Kir3 channels with the exception of Kir6.2-P69 and H175, which in Kir2 and Kir3 are an arginine and a lysine, respectively, and shown to coordinate PIP_2 binding [16-19]. The amino acid difference at these two positions would weaken Kir6.2-PIP_2 interactions, consistent with the lower phosphoinositide head-group specificity compared to other Kir channels [38]. The Kir6.2-H175 side chain could be modeled in two rotamer positions in the map: one oriented towards PIP_2 in the conserved binding site and the other towards E179 in the same Kir6.2 subunit (Fig. 2B). Kir6.2-H175 has been previously implicated in proton sensing in K_{ATP} channels [39]. Between pH 6.4-7.4, K_{ATP} channel activity exhibits biphasic pH dependence, with peak activity at ~pH 6.7; mutating Kir6.2-H175 to lysine increased basal channel activity and abolished channel sensitivity to pH, leading to the suggestion that the H175K mutation may increase channel interaction with PIP_2 [39]. The ability

of Kir6.2-H175 to act as a proton sensor also depends on Kir6.2-E179; mutating E179 to Q diminished the pH response of the channel [39, 40]. Our structural observation suggests H175 undergoes pH-dependent switch between two rotamers (see Fig. 2B). At mild acidic pH, a bi-protonated imidazole sidechain interacts with PIP_2 to increase channel opening, while at basic pH, a neutral state imidazole sidechain interacts with Kir6.2-E179 to reduce PIP_2 interaction, hence reducing channel opening.

The second PIP_2 molecule sits in a novel site coordinated by both Kir6.2 and SUR1 subunits (Figs.1B, 2A-C). Here, the PIP_2 head group interacts with surrounding residues including K39 and Q57 of Kir6.2, and N131, F132, P133, and K134 of SUR1. Previously we have noted that in closed K_{ATP} structures, SUR1-K134, located in ICL2 of SUR1-TMD0, has its side chain directed towards cryoEM densities in the predicted PIP_2 binding pocket tentatively assigned as phosphatidylserines [36]. Based on the observation, we mutated SUR1-K134 to alanine and found it reduced channel P_o, which was recovered by adding exogenous PIP_2 [36]. Our PIP_2-bound open structure now shows that SUR1-K134 is involved in PIP_2 binding but at the novel second site, directly explaining the mutational study result.

Structural interactions with the acyl chains of PIP_2

Most phospholipids present a range of molecular species comprising acyl chains of diverse length and saturation [14]. However, mammalian PIPs show the predominance of a single hydrophobic backbone composed of arachidonoyl (20:4) and stearoyl (18:0) chains [37]. In the open K_{ATP} channel structure determined with an enrichment of natural brain PIP_2 in the membrane, we observed cryoEM densities corresponding to branched long acyl chains for both PIP_2 molecules (Figs. 2B, S3A, S3B). The first PIP_2 bound at the Kir-conserved site, mediates interactions between Kir6.2 subunits. While one acyl chain is primarily associated with the outer TM helix of the Kir6.2 subunit that coordinates head group binding, the other chain sits between the outer

helicies of two adjacent Kir6.2 subunits (Fig. 2B). CryoEM density at this conserved PIP_2 binding pocket was previously reported by our group and others, but in those studies the map features lack lipid acyl tails and could not be ascertained as PIP_2 [28, 34, 35, 41]. The lipid tails of the second PIP_2 molecule are sandwiched between TM1 and TM4 of SUR1-TMD0 and TMs of Kir6.2, and have non-polar interactions with SUR1 (V34, F38, I42, P45, I46, L135, I137, A138, I141) and Kir6.2 (L56, V59, I159) (Fig. 2B, C). Long-chain PIP_2 stably activates K_{ATP} channels [11, 12]; in contrast, activation of channels by synthetic short chain PIP_2 such as diC8-PIP_2 is readily reversible [38]. The extensive hydrophobic interactions between channel subunits and the long acyl chains of 18:0/20:4 PI(4,5)P_2 observed in our structure provide an explanation for the apparent increase in stability of long-chain PIP_2.

Functional role of the two PIP_2 binding sites

To probe the functional role of the two PIP_2 binding sites, we compared the PIP_2 response of wild-type (WT) channels to channels containing the following mutations: Kir6.2-R176A, which disrupts the conserved PIP_2 binding site; SUR1-K134A, which disrupts the novel PIP_2 binding site; Kir6.2-R176A and SUR1-K134A, which disrupt both PIP_2 binding sites (Fig. 2B,C). Exposure to PIP_2 increased activity and decreased ATP inhibition over time in all channels (Fig. 2D). However, the initial currents upon membrane excision, the extent of current increase upon PIP_2 stimulation, and the PIP_2 exposure time required for currents to reach maximum, showed striking differences among the different channels. WT channels exhibited robust activity upon membrane excision into ATP-free solution, and currents increased by 1.48 $\pm$ 0.23-fold (Fig. 2E) that plateaued within one minute of PIP_2 exposure. Perturbation of the second PIP_2 binding site by the SUR1-K134A mutation resulted in channels that showed reduced initial currents, which increased by 3.96 $\pm$ 0.47-fold in response to PIP_2. Perturbation of the first PIP_2 binding site by the Kir6.2-R176A mutation markedly reduced initial currents, which increased by 48.74 $\pm$ 18.25-fold after PIP_2

exposure. Combining both SUR1-K134A and Kir6.2-R176A yielded channels that showed barely detectable currents at patch excision and a dramatic 299.65 ± 121.72-fold current increase by PIP_2. All three mutants also required longer PIP_2 exposure to reach maximum currents in the order of double mutant > Kir6.2-R176A > SUR1-K134A (see Fig. 2D). These results demonstrate that both PIP_2 binding sites have functional roles in K_{ATP} channel activity.

Kir6.2 pore in open conformation

In Kir channels, there are three constriction points in the K^+ conduction pathway: the selectivity filter on the extracellular side, the inner helix gate at the helix bundle crossing where four inner helices (M2) converge, and the G-loop gate in the cytoplasmic pore just below the membrane [13]. The structure of the SUR1/Kir6.2^{Q52R} K_{ATP} has an open Kir6.2 inner helix gate (Fig. 3). Clear cryoEM density shows rotation of the Kir6.2-F168 side chains away from the pore's center, thus causing a dilated pore size (Figs.3, 4A, movie 1). The radius of the K^+ pathway at the inner helix gate is ~3.3 Å, compared to ~0.5 Å in the WT K_{ATP} channel bound to inhibitors we reported previously [34, 41], exemplified by the ATP and repaglinide (RPG) bound structure (PDB ID 7TYS) [41] (Fig. 3). The radius at the inner helix gate in our current structure is comparable to that in the open structure of SUR1/Kir6.2^{C166S,G334D} (3.3 Å) [27], and the pre-open structure of SUR1-Kir6.2^{H175K} fusion channel (3.0 Å) [28]. In contrast to the inner helix gate, little difference is observed in the G-loop gate between closed and open structures, suggesting minimum involvement of the G-loop gate in K_{ATP} channel gating.

The SUR1/Kir6.2^{Q52R} K_{ATP} sample was purified in the absence of nucleotides; as expected, no ATP cryoEM density was observed at the inhibitory ATP-binding site on Kir6.2. Nonetheless, the open conformation includes structural rearrangements at the ATP binding site that would disfavor ATP binding (Fig. 4B,C). Specifically, the sidechains of Kir6.2-K39 and R50 flip away from ATP-interacting positions, with the K39 sidechain now coordinating PIP_2 at the second site;

moreover, the sidechain of Kir6.2-E51 forms an intramolecular hydrogen bond with R54 to partially occlude the ATP binding pocket (Fig. 4B). Our observation agrees with previous hypotheses that the open channel conformation is not compatible with ATP binding at Kir6.2 and that ATP inhibits the channel by stabilizing the channel in the closed conformation [15].

Relative to channels bound to inhibitors, in which the cytoplasmic domain (CTD) of Kir6.2 is predominantly positioned close to the plasma membrane ("up" conformation) [41], the SUR1/Kir6.2^{Q52R} open channel structure shows the Kir6.2-CTD is also juxtaposing the membrane but further rotated clockwise (viewed from the extracellular side) (Fig.4A). This twisting as well as the other aforementioned structural changes at the ATP binding site are similarly observed in the open structure of SUR1/Kir6.2^{C166S,G334D} [27], and the pre-open structure of SUR1-Kir6.2^{H175K} [28]. The converging observations in three open structures using different mutant constructs suggest WT K_{ATP} channels undergo similar conformational changes between closed and open states.

Analysis of SUR1 structure

Since no nucleotides were added to the SUR1/Kir6.2^{Q52R} sample, no ATP or ADP density at the NBDs of SUR1 was observed. The two NBDs were clearly separated but not well resolved; in particular, NBD2 is highly dynamic with a local resolution > 5 Å (Fig. 1, S2). The N-terminal domain of Kir6.2 (the distal 30 amino acids, referred to as KNtp) was absent from the central cleft lined by TM helices from TMD1 and TMD2 of the SUR1-ABC core even when the map was filtered to low resolution (6 Å; see Fig.S4). Presence of KNtp in the SUR1-ABC core has been linked to channel inhibition [35, 36, 42], the lack of KNtp density in the SUR1-ABC core is therefore predicted in the SUR1/Kir6.2^{Q52R} open channel structure. No continuous density corresponding to KNtp was observed at an alternative site to suggest a stable resting position when in the open conformation, precluding structural modeling of this flexible domain.

The ABC modules of the four SUR1 subunits in the SUR1/Kir6.2^{Q52R} map from a C4 non-uniform refinement adopt a propeller-like conformation (Fig. 1A, B). Further 3D classification of the symmetry expanded particle set revealed SUR1 dynamics with 3 distinct rotational positions of SUR1-ABC module relative to the Kir6.2-SUR1-TMD0 tetrameric core (Fig. S5). The conformational dynamics of the SUR1-ABC module are similar to those reported in the SUR1 NBDs-dimerized, open structure of the SUR1/Kir6.2^{C166S,G334D} channel [27], thus likely represent intrinsic flexibility of this domain regardless of nucleotide binding and/or NBD dimerization.

Compared to inhibitor-bound closed Kir6.2/SUR1 channel structures [reviewed in [6, 7]], SUR1 subunits in the SUR1/Kir6.2^{Q52R} open structure are more tilted away from Kir6.2 and elevated towards the plasma membrane (viewed from the side) such that they are nearly in plane with the Kir6.2 tetramer (compare Fig. 1B and 1C). Accompanying this upward SUR1 motion, there is an overall rigid-body rotation of SUR1 driven by a rotation of the TMD0 of SUR1 in the open structure relative to closed structures (Fig. 5). At the outer leaflet, SUR1-F41, which interacts with Kir6.2-L84 in the closed conformation, now interacts with Kir6.2-L85 in the open conformation (Fig. 5C). At the inner leaflet, TMD0 moves away from Kir6.2 (Fig. 5A, 5C), creating a space between SUR1-TM1 and Kir6.2-M1. Using PISA analysis [43], the contact surface area at this interface (between SUR1-TM1 residues 27-54 and Kir6.2-M1 residues 66-96) is 645.6 $Å^2$ (ΔG = -20 kcal/mol) in the closed channel structure (PDB ID: 6BAA), which is reduced to 395.9 $Å^2$ (ΔG = -12 kcal/mol) in the SUR1/Kir6.2^{Q52R} open structure. Binding of a second PIP_2 in this space (see Fig.2B) compensates for the lost surface contact between SUR1-TMD0 and Kir6.2, thus stabilizing this interface in the open channel.

Similar structural changes are also seen in the pre-open SUR1-Kir6.2^{H175K} fusion structure where SUR1 NBDs are bound to Mg-ATP/ADP and dimerized [44]. Dimerization of SUR1 NBDs

antagonizes ATP inhibition at Kir6.2 and stimulates K_{ATP} channel activity. It has been proposed that NBD dimerization causes outward bending of the cytoplasmic half of SUR1-TMD0 and the pulling away of K205 in SUR1-L0 from binding ATP at the inhibitory site to stimulate channel activity [44]. Since our open SUR1/Kir6.2^{Q52R} structure does not contain Mg-ATP/ADP and the NBDs are clearly separated, the similar conformational changes we observed at SUR1-TMD0/L0 are not driven by SUR1 NBD dimerization. One possibility is that MgATP/ADP and PIP_2 converge on the same structural mechanism to open the channel, as has been proposed previously based on functional studies [45].

Kir6.2-Q52R stabilizes the open conformation by interacting with SUR1-W51

Kir6.2-Q52 is located immediately N-terminal to the interfacial helix (IFH; a.k.a. slide helix) and C-terminal to βA (Fig. 4B, 4C). In published ATP-bound closed structures, Kir6.2-Q52 lies close to SUR1-E203 in the proximal portion of the SUR1-L0 linker (Fig. 4C). Previous studies have shown that enforcing Kir6.2-Q52 and SUR1-E203 interactions via engineered charged amino acid pair or cysteine crosslinking reduced ATP inhibition IC_{50} by 100-fold or caused spontaneous channel closure in the absence of ATP, respectively [46]. These results indicate that stabilizing the interface between Kir6.2 βA-IFH and SUR1-L0 stabilizes ATP binding and channel closure. In contrast, in the SUR1/Kir6.2^{Q52R} open structure, the SUR1-L0 linker moves ~8 Å towards SUR1 and away from the ATP-binding site on Kir6.2 (Fig. 4A), with SUR1-E203 and K205 flipped away from Kir6.2 such that SUR1-TMD0 ICL1 (aa 52-60) engages with Kir6.2-βA to form a main chain β-sheet (Fig. 4B). In particular, the sidechain of Kir6.2 residue 52 (Q in WT, R in mutant) now faces SUR1-TMD0 and interacts with SUR1-W51 (Fig. 4B), tethering the Kir6.2-CTD to SUR1-TMD0 in a rotated open position.

The Kir6.2-Q52R mutation increases P_o and decreases ATP inhibition of K_{ATP} channels in a SUR1-dependent manner [47]. The cation-π interaction observed between Kir6.2-Q52R and

SUR1-W51 in the open conformation (Fig. 6A) led us to hypothesize this interaction underlies the gain-of-function gating effect of the Kir6.2-Q52R mutation, by stabilizing Kir6.2-CTD in a rotated open conformation. To test this, we mutated W51 of SUR1 to cysteine and assessed the ATP sensitivity of channels formed by co-expressing Kir6.2^{Q52R} and SUR1^{W51C} using inside-out patch-clamp recording. The SUR1-W51C mutation reversed the effect of the Kir6.2-Q52R mutation on ATP sensitivity of the channel to resemble WT channels (Fig. 6B). The IC_{50} values of ATP inhibition for WT, SUR1/Kir6.2^{Q52R}, SUR1^{W51C}/Kir6.2, and SUR1^{W51C}/Kir6.2^{Q52R} channels are 8.9 ± 0.6 μM, 168.4 ± 74.9 μM, 21.6 ± 4.9 μM, and 5.2 ± 0.4 μM, respectively (Fig. 6C). Corroborating these findings, in Rb^+ efflux assays cells co-expressing Kir6.2^{Q52R} and SUR1^{W51C} showed efflux levels similar to cells expressing WT channels, in contrast to the significantly higher efflux in cells co-expressing Kir6.2^{Q52R} and WT-SUR1 (Fig. 6D). These results provide strong evidence that Kir6.2-Q52R interacts with SUR1-W51 to enhance channel activity and reduce ATP inhibition, thus explaining the SUR1-dependent pathophysiology of this neonatal diabetes mutation.

Discussion

In this study, we surmounted the technical difficulties in capturing PIP_2 bound to K_{ATP} channel, firstly by using a neonatal-diabetes Kir6.2 variant known to enhance channel activity, and secondly by using naturally occurring long chain PIP_2 before membrane solubilization, rather than the previously used approach of adding short chain synthetic PIP_2 after purification of channels [23, 44, 48]. The excellent cryoEM map quality permitted confident assignment of the PIP_2 densities. The tandem PIP_2 binding sites coordinated by Kir6.2 itself and its regulatory subunit SUR1 uncovers an unprecedented cooperation between an ion channel and transporter on PIP_2 binding, and highlights the uniqueness of the K_{ATP} complex in the evolution of K^+ channels and ABC proteins. The structure resolves a major problem in the long-standing puzzle of how SUR1, in particular TMD0 of SUR1, modulates the open probability of the Kir6.2 channel [24, 25].

Moreover, it answers a long-standing question of how a prominent clinical Kir6.2 mutation increases channel activity to cause neonatal diabetes [47].

Unique PIP_2 binding pocket in K_{ATP} channels

As a member of the Kir channel family, Kir6.2 was expected to contain a conserved PIP_2 binding site, akin to that identified in Kir2 and Kir3 [16-19]. Our structure confirms that this is indeed the case. Surprisingly, our structure reveals a second, novel PIP_2 binding site immediately next to the conserved Kir channel PIP_2 binding site. This second site is uniquely coordinated by both SUR1 and Kir6.2 subunits. Mutational studies support functional importance of PIP_2 binding at both sites [41] (Fig. 2D, E). In single channel recordings, Kir6.2 channels without SUR1 have low P_o with brief openings, in contrast to Kir6.2 channels assembled with SUR1 or SUR1-TMD0, which exhibit ~10-fold higher P_o and long bursts of openings [15, 24, 25, 49]. We propose the low P_o and brief openings in Kir6.2 channels lacking SUR1 result from PIP_2 binding at the conserved site, which tethers Kir6.2-CTD near the membrane to rotate to the open position. PIP_2 binding at this ancestral site may not be as strong as in Kir2 and Kir3 channels due to sequence variations at key residues including Kir6.2 P69 and H175 (both lysines in Kir2 and 3) [16-19], explaining the low P_o of Kir6.2. PIP_2 binding at the unique novel site formed by SUR1 and Kir6.2 enables SUR1 to stabilize the Kir6.2-CTD in the rotated open position, giving rise to bursts of openings and higher P_o.

The PIP_2 binding pocket is smaller in the closed structure than in the open structure. In a solvent accessible surface representation of the model for closed structure, PIP_2 at the second site would clash with SUR1 (Fig. S6). This implies that PIP_2 moves in and out of the second site as the channel opens and closes. In our published closed structures without exogenous PIP_2, there was also lipid density, which we tentatively modeled as two phosphatidylserines [36]. We speculate that this pocket may accommodate different lipids as the channel transitions between

closed and open conformations. Further studies are required to elucidate the binding order of PIP_2 molecules, but the first PIP_2 binding site appears available in both the open and closed channel conformations (Fig. S6).

K_{ATP} channels exhibit lower specificity towards PIPs compared to other Kir channels, and are activated equally well by $PI(4,5)P_2$, $PI(3,4)P_2$, and $PI(3,4,5)P_3$, and also by PI(4)P and long chain (LC)-CoAs [38]. The structural basis underlying the reduced PIPs specificity for K_{ATP} channel activation requires further investigation, but the large size of the binding pocket may accommodate different PIPs and LC-CoAs. Such degeneracy may account for the observation that purified K_{ATP} channels reconstituted in lipid bilayers lacking PIP_2 exhibited spontaneous single channel openings [27], in contrast to Kir2 and Kir3 channels which require PIP_2 for activity [19, 50].

Mechanism of PIP_2 and ATP antagonism

PIP_2 and ATP functionally compete to open or close K_{ATP} channels (Fig. 2D) [11, 12]. Kinetic analyses have indicated that PIP_2 and ATP binding are mutually excluded [15]. Comparison between PIP_2 bound SUR1/Kir6.2^{Q52R} open structure and previously published ATP-bound closed structures shows PIP_2 and ATP antagonism occurs via both binding competition and allosteric mechanisms (Fig.4, movies 1, 2). At the level of binding competition, both ligands compete for a common binding residue, Kir6.2-K39, which interacts with ATP in the ATP-bound closed structures [34, 36] but with PIP_2 in the PIP_2-bound open structure (Fig.2B). Previous MD simulations using ATP-bound closed structures of Kir6.2 tetramer [51] or tetramer of Kir6.2 plus SUR1-TMD0 [36] with a single PIP_2 molecule docked in the conserved PIP_2 binding site found that Kir6.2-K39 [51] or both K39 and R54 [36] switched between ATP binding and PIP_2 binding. In the SUR1/Kir6.2^{Q52R} open structure, we see Kir6.2-K39, rather than binding PIP_2 in the conserved site, binds the second PIP_2 in the novel site (Fig.2B). In contrast, Kir6.2-R54 is not

involved in PIP_2 binding; instead, it hydrogen bonds with Kir6.2-E51 in the same subunit and E179 in the adjacent Kir6.2 subunit, which stabilizes the interface between the IFH and the C-linker helix in the open conformation. Mutation of both K39 and R54 to alanine has been shown to reduce ATP as well as PIP_2 sensitivities [52]. Our structure clarifies the structural role of K39 and R54 and suggests while K39A likely reduces PIP_2 sensitivity by weakening PIP_2 binding at the novel site, R54A likely reduces PIP_2 sensitivity indirectly by disrupting interactions in Kir6.2 that are needed to stabilize the open channel conformation.

Allosterically, PIP_2 binding diverts ATP binding residues away from the ATP binding pocket to disfavor ATP binding. These include sidechain reorientation of Kir6.2 K39 and R50, and interaction between Kir6.2 R54 and E51 that partially occludes the ATP binding pocket (Fig.4B). Moreover, in the ATP-bound closed conformation, SUR1-L0 interfaces with Kir6.2-βA, allowing SUR1-K205 to coordinate ATP binding [36, 42, 46, 53] and stabilize channel closure. However, in the open structure, SUR1-L0 is disengaged from Kir6.2-βA, allowing Kir6.2-CTD to rotate such that ICL1 of SUR1-TMD0 engages with Kir6.2-βA, forming a continuous β-sheet to stabilize the open conformation, which also disfavors ATP binding. Similar changes have been described in recently published SUR1/Kir6.2$^{C166S,\ G334D}$ open structure [27] and SUR1-Kir6.2^{H175K} fusion pre-open structure [44]. The common structural rearrangements from closed to open state seen independent of mutations support the same gating transition in WT channels and highlight a key role of SUR1 in stabilizing the Kir6.2-CTD in two distinct rotational positions to close or open the K_{ATP} channel.

Insights on disease mutations

The study provides mechanistic insight on how Kir6.2-Q52R causes neonatal diabetes. The strong cation-π interaction engendered by the Kir6.2-Q52R mutation with SUR1-W51 illustrates how changes at this interface have profound effects on channel gating and physiology. Inspection

of the published SUR1/Kir6.2^{G334D,C166S} open structure and the SUR1-Kir6.2^{H175K} fusion channel pre-open structure reveals the Kir6.2-Q52 residue is similarly in position to interact with SUR1-W51 [27, 28]. The polar-π interaction between glutamine and tryptophan is much weaker than the cation-π interaction between arginine and tryptophan. The difference in binding energy for the relevant gas-phase interactions for polar-π is 1.4 kcal/mol (NH_3-Benzene), compared to the cation-π interaction energy of 19.0 kcal/mol (NH_4^+-Benzene) [54, 55]. That wild-type and Kir6.2-Q52R both interact with SUR1-W51 suggest an important role of Kir6.2-Q52 in stabilizing Kir6.2-CTD and SUR1-TMD0 interface for channel opening.

In addition to Kir6.2-Q52R, many disease mutations are located at the SUR1-Kir6.2 interface seen in the SUR1/Kir6.2^{Q52R} open structure (Fig. 7). These include congenital hyperinsulinism (HI) associated loss-of-function mutations Kir6.2-R54C, L56G, K67D, R176H and R177 and SUR1-I46T, P133R, and L135V, as well as neonatal diabetes (ND) and Developmental delay, Epilepsy, and Neonatal Diabetes (DEND) syndrome associated gain-of-function mutations Kir6.2-K39R, E51A/G, Q52R/L. G53D/N/S/R/V, V59A/G/M, W68C/G/L, K170N/R/T, E179A/K, and SUR1-P45L, I49F, F132L/V, and L135P (Fig. 7) [56]. Some of these, such as HI-associated K67D and R176H, and ND/DEND associated K39R, W68C/G/L involve residues that coordinate PIP_2 binding; others however, likely exert allosteric effects to affect PIP_2 or ATP gating indirectly by stabilizing channels in closed or open conformations.

In summary, the PIP_2-bound K_{ATP} channel structure elucidates the intimate partnership between SUR1 and Kir6.2 in coordinating PIP_2 binding and channel gating. The unique PIP_2 binding pocket and the molecular interactions involved in gating provide a framework for designing new K_{ATP} modulators to control channel activity. The finding that SUR1 binds PIP_2 to regulate

Kir6.2 also raises the question whether PIP_2 serves structural and functional roles in other ABC proteins, as has been implicated for CFTR [57].

Materials and methods

Cell lines

COSm6 cells were cultured in high-glucose DMEM medium (GIBCO) supplemented with 10% Fetal Bovine Serum (Fisher Scientific), 100 U/mL penicillin, and 100 U/mL streptomycin at 37°C with 5% CO_2.

Protein expression and purification

Genes encoding rat Kir6.2-Q52R and N-terminal FLAG-tagged (DYKDDDDK) hamster SUR1 were cloned into pShuttle vectors and then the AdEasy vector (Stratagene), and packaged into recombinant adenoviruses, which were used for protein expression as described previously [58]. However, instead of inducing K_{ATP} channel expression in INS-1 cells, which are pancreatic beta cell derived and have endogenous WT Kir6.2 and SUR1 expression that would mix with the Q52R variant, a different mammalian adhesion cell line was used (COSm6 cells). COSm6 cells grown to mid-log in 15 cm tissue-culture plates were infected with adenoviruses packaged with Kir6.2, SUR1, and tTA, using multiplicity of infections (MOIs) optimized empirically. Note the pShuttle vector used for SUR1 contains a tetracycline-regulated response element, necessitating co-infection of a tTA (tetracycline-controlled transactivator) adenovirus for SUR1 expression. At ~24 hours post-infection, cell medium was changed and included 100 μM tolbutamide post-infection. Tolbutamide enhances K_{ATP} channel expression at the plasma membrane and washes out easily. At ~48 hours post-infection, cells were harvested by scraping and cell pellets were frozen and stored at -80°C until purification.

SUR1/Kir6.2^{Q52R} channels were purified similar to previously described [58], except after the total membrane fraction was prepared, membranes were re-suspended in buffer containing 0.2 M NaCl, 0.1 M KCl, 0.05 M HEPES pH 7.5, 4% trehalose, and 1 mg/mL brain PIP_2 (Avanti Polar Lipids), and incubated at 4°C for 30 minutes before increasing the volume 10x in the same buffer without added lipids but including the detergent digitonin at a final concentration of 0.5%, then membranes were solubilized at 4°C for 90 minutes. As previously described [58], after clarification by ultracentrifugation, the soluble fraction was incubated with anti-FLAG M2 affinity agarose for 10 hours and eluted at 4°C for 60 minutes with a buffer containing 0.2 M NaCl, 0.1 M KCl, 0.05 M HEPES pH 7.5, 0.05% digitonin and 0.25 mg/mL FLAG peptide. Purified channels were eluted at ~170nM (~150 μg/ml) and used immediately for cryo-EM grid preparation. K_{ATP} channel particles were also fixed and stained using Uranyl Acetate and sample quality was assessed by negative-stain-EM.

CryoEM sample preparation and data acquisition

To increase protein adsorption to the cryoEM grids, and also to mitigate selective-orientation of K_{ATP} channel particles that occurs on commercial carbon surfaces, graphene-oxide (GO) grids were prepared as previously described [59]. Briefly, gold Quantifoil R1.2/1.3 400 mesh grids were cleaned with acetone and glow-discharged for 60 seconds at 15 mA with a Pelco EasyGlow®, and 4 µL of 1 mg/mL Polyethylenimine (PEI, 40,000 MW) in 25 mM HEPES pH 7.9 was applied to each grid and incubated for 2 minutes followed by washing with water. Then, 0.1 mg/ml GO was vortexed vigorously and applied to the grid and incubated for 2 minutes followed by two washes with water. The GO grids were allowed to dry for 15 minutes and used within 2 hours for sample vitrification.

To prepare cryoEM samples, 3 µL of purified K_{ATP} channel complex was loaded onto fresh GO-coated grids for 30 s at 6 °C with a humidity of 100%. Grids were blotted for 2.5 seconds with a blotting force of -10 and cryo-plunged into liquid ethane cooled by liquid nitrogen using a Vitrobot Mark III (FEI).

Single-particle cryo-EM data was collected on a Titan Krios 300 kV cryo-electron microscope (ThermoFisher Scientific) in the Pacific Northwest CryoEM Center (PNCC), with a multi-shot strategy using beam shift to collect 27 movies per stage shift, assisted by the automated acquisition program SerialEM. Images were recorded on the Gatan K3 Summit direct-electron detector in super-resolution mode, post-GIF (20eV window), at 105,000x magnification (calibrated image pixel-size of 0.826 Å; super-resolution pixel size 0.413 Å); nominal defocus was varied between -1.0 and -2.5 µm across the dataset. The dose rate was kept around 24 $e^-/Å^2$/sec, with a frame rate of 35 frames/sec, and 78 frames in each movie (i.e. 2.2 sec exposure time/movie), which gave a total dose of approximately 55 $e^-/Å^2$. Three grids that were prepared in the same session using the same protein preparation were used for data collection, and from these three grids, 2727, 3956 and 1576 movies (8,259 movies total) were recorded.

CryoEM image processing

Super-resolution dose-fractionated movies were gain-normalized by inverting the gain reference in Y and rotating upside down, corrected for beam induced motion, aligned, and dose-compensated using Patch-Motion Correction in cryoSPARC2 [60] without binning. Parameters for the contrast transfer function (CTF) were estimated from the aligned frame sums using Patch-CTF Estimation in cryoSPARC2 [60] and binned by 2 with Fourier cropping. Micrographs were manually curated using sorting by curate exposures. The resulting 5241 dose-weighted motion-corrected summed micrographs were used for subsequent cryo-EM image processing. Particles were picked automatically using template-based picking in cryoSPARC2 based on 2D classes

obtained from cryoSPARC live during data collection. For each of the three sets of data, particles were cleaned by three rounds of 2D classification in cryoSPARC2 [60]. The combined particle stack contained 70,638 particles, which were then used for ab initio reconstruction in C1 requesting two classes. Only classes that had good alignments and contained full channel particles were included in subsequent rounds of classification. 40,896 particles from the best class were then subjected to ab initio reconstruction in C1 requesting three classes, which gave a class with only side, a class with only top/bottom, and a good class with 23,378 particles. These 23,378 particles were used for a final ab initio reconstruction using three classes, and gave 21,663 particles that sorted into a class with a straight transmembrane region (14,992 particles) and a class where the transmembrane region was more bent with the Kir6.2 core puckered up towards the extracellular space (6,657 particles). Further rounds of ab initio reconstruction resulted in equivalent classes without further improvement in particle classification. The particles were re-extracted using a 600 pixel box at 0.826 Å/pix, duplicate particles within 20 Å from each other on the micrograph were removed, then used as input for non-uniform refinement [61] in C1 with the 6,657 particle map reconstruction at 6.4 Å resolution and the 14,115 particle map reconstruction at 3.4 Å resolution. A non-uniform refinement in C4 symmetry imposed with the 14,115 particles resulted in a 2.9 Å resolution reconstructed cryoEM map using cryoSPARC auto mask tightening (Figs. S1, S2). The auto-tightened FSC mask excluded the disordered NBD2 (Fig. S2B). Masks for FSC calculation that included the full K_{ATP} channel with or without micelle were generated using molmap in ChimeraX [62] (Fig. S2B), and resampled on the full map grid (600^3 pixels). The FSC calculated using these static masks yielded 3.3 Å resolution for the full channel without micelle (Fig.S2A) and 3.5 Å resolution for the entire particle including the micelle ("Loose" in the FSC plot shown in Fig. S1).

To assess conformational heterogeneity within the high-resolution class of 14,115 particles of full-channel complexes that may have individual SUR1 subunits adopting independent

conformations within a single K_{ATP} channel particle, particles were subjected to C4 symmetry expansion. A mask covering the Kir6.2 tetramer, four TMD0 densities in SUR1, plus a large volume surrounding one of the SUR1 subunits, to have a large region covering all possible SUR1 locations, was generated using Chimera and used as a focused map to conduct 3D classification without particle alignment in cryoSPARC2. A mask that covered three of the SUR1 subunits was used for signal subtraction implemented in cryoSPARC. An initial focused 3D classification searching for 5 classes sorted particles into three dominant classes (class 0: 925 particles; class 1: 22474 particles; class 2: 10711 particles; class 3: 25664 particles; class 4: 194 particles). Class 1 to 3 showed three distinct SUR1 conformations, and subsequent local refinement using a loose mask covering the Kir6.2 tetramer, four TMD0 domains of SUR1, and one SUR1, resulted in map reconstructions of 3.12 Å, 3.99 Å, and 3.07 Å resolutions for class 1, 2, and 3, respectively. Combined particles from these three classes were subjected to non-uniform local refinement and resulted in 2.9 Å resolution cryo-EM map reconstructions [61], reproducing the C4 non-uniform refinement of the particle classes before symmetry expansion. In all three of these particle classes, the NBDs are separated, but with substantial differences between the relative positions of NBD2, and better resolved maps corresponding to the NBD2 than for the overall consensus C4 non-uniform refinement. For all cryo-EM maps, the mask-corrected Fourier shell correlation (FSC) curves were calculated in cryoSPARC2, and the resolutions were reported based on the 0.143 criterion [63]. The results of 3D classification in cryoSPARC showed highly dynamic motions of SUR1 (Fig.S5) and the local resolution analysis showed corresponding lower local resolution of the highly dynamic NBDs of SUR1 (Fig. S2C) [64].

In the C4 reconstruction of the full K_{ATP} channel particle, there is good density for nearly every side chain of Kir6.2 except for the N-terminal 31 residues and the C-terminal residues beyond residue 352. TMD0 and the transmembrane helicies of SUR1 also have clear density, with unclear density for the dynamic NBDs and loop regions, especially NBD2 which is poorly

resolved due to apparent high flexibility when in the open conformation without NBD dimerization conditions.

To create an initial structural model, PDB ID 6BAA was fit into the reconstructed density for the full K_{ATP} channel particle using Chimera [65], and then refined in Phenix [66] as separate rigid bodies corresponding to TMD (32-171) and CTD 172-352) of Kir6.2 and TMD0/L0 (1-284), TMD1 (285-614), NBD1 (615-928), NBD1-TMD2-linker (992-999), TMD2 (1000-1319) and NBD2 (1320-1582). All sidechains and missing loops that had clear density were then built manually using Coot [67]. The resulting model was further refined using *Coot* and *Phenix* iteratively until the statistics and fitting were satisfactory (Table S1). Two models are presented. The first (PDB ID 8TI2) contains residues 32-352 for Kir6.2, and residues 1-1578 for SUR1 except for an extracellular loop (1043-1060), two loop regions (623-673 and 743-766) in NBD1 and the linker between NBD1 and TMD2 (928-986). The second model (PDB ID 8TI1) has the highly flexible NBD2 removed, and the SUR1 model ends at residue 1317. NBD1/2 and loop regions showed signs of disorder, thus many sidechains of residues in these regions were stubbed at Cβ. The N-terminal of Kir6.2, which in the closed NBD-separated conformation rests between TMD1 and TMD2 of SUR1, is not observed in this conformation.

In addition to protein density, two N-acetylglucosamine (NAG) molecules per SUR1 monomer, which are common cores of N-linked glycosylation, are modeled in the distinctively large density at the side chain of SUR1-N10. Densities corresponding to two PIP_2 molecules were also observed at the interface between Kir6.2 and SUR1 and were modeled after considering fits of other lipid molecules. Three other lipid sites per SUR1 monomer provided a useful contrast to the bulky density of the PIP_2 head group (Fig. S3). The resulting model was further refined using *Coot* [67] and *Phenix* [66, 68, 69] iteratively until the statistics and fitting were satisfactory (Table S1). All structure figures were produced with UCSF Chimera [65],

ChimeraX[62], and PyMol (http://www.pymol.org). Pore radius calculations were performed with HOLE implemented in *Coot* [67].

Electrophysiology

For electrophysiology experiments, COSm6 cells were co-transfected with various combination of WT or mutant SUR1 and Kir6.2 cDNAs along with the cDNA for the Green Fluorescent Protein (to facilitate identification of transfected cells) using FuGENE® 6. Cells were plated onto glass coverslips twenty-four hours after transfection and recordings made in the following two days. All experiments were performed at room temperature as previously described [70]. Micropipettes were pulled from non-heparinized Kimble glass (Fisher Scientific) on a horizontal puller (Sutter Instrument, Co., Novato, CA, USA). Electrode resistance was typically 1-2 MΩ when filled with K-INT solution containing 140 mM KCl, 10 mM K-HEPES, 1 mM K-EGTA, 1 mM EDTA, pH 7.3. ATP was added as the potassium salt. Inside-out patches of cells bathed in K-INT were voltage-clamped with an Axopatch 1D amplifier (Axon Inc., Foster City, CA). ATP or porcine brain PIP_2 (Avanti Polar Lipids; prepared in K-INT and bath sonicated in ice water for 30 min before use) were added to K-INT as specified in the figure legend. All currents were measured at a membrane potential of -50 mV (pipette voltage = +50 mV). Data were analyzed using pCLAMP10 software (Axon Instrument). Off-line analysis was performed using Clampfit and GraphPad. Data were presented as mean ± standard error of the mean (S.E.M). ATP inhibition dose-response curves were obtained by fitting data to the Hill equation ($I_{rel} = 1/(1 + ([ATP]/IC_{50})^H)$), where Irel is the current relative to the maximum currents in K-INT solution (expressed as % current in Fig. 6C), IC_{50} is the ATP concentration that causes half-maximal inhibition, and H is the Hill coefficient. Note H was allowed to vary for the curves shown in Fig. 6C.

Rb^+ efflux assay

COSm6 cells were transiently transfected with various combination of WT or mutant SUR1 and Kir6.2 cDNAs using FuGENE® 6. Untransfected cells were included as background control. Cells were cultured in medium containing 5 mM RbCl overnight. The next day, cells were washed quickly twice in Ringer's solution (5.4 mM KCl, 150 mM NaCl, 1 mM $MgCl_2$, 0.8 mM NaH_2PO_4, 2 mM $CaCl_2$, 25 mM HEPES, pH 7.2) with no RbCl. Rb efflux was measured by incubating cells in Ringer's solution over a 40 min period. At the end of the 40 min incubation, Ringer solution was collected and cells lysed in Ringer's solution plus 1% Triton X-100. Rb concentrations in both the efflux solution and cell lysate were measured using an Atomic Adsorption Instrument Ion Channel Reader (ICR) 8100 from Aurora Biomed. Percent efflux was calculated by dividing Rb in the efflux solution over total Rb in the efflux solution and cell lysate. For each experiment, duplicates were included as technical repeats and the average taken as the experimental value. For all channel combinations, five separate transfections were carried out in parallel as biological repeats. Data were presented as mean ± standard error of the mean (S.E.M) and statistical analysis performed by one-way ANOVA with Tukey post hoc test in GraphPad.

Data availability

The cryo-EM maps have been deposited in the Electron Microscopy Data Bank (EMDB), and the coordinates have been deposited in the PDB under the following accession numbers: PDB ID 8TI2 and EMD-41278 (NBD2 modeled as main chain atoms only); PDB ID 8TI1 and EMD-41277 (NBD2 not modeled).

Conflict statement

The authors declare that they have no competing financial or non-financial interests with the contents of this article.

Author contributions

CMD designed and performed experiments, analyzed data, prepared figures, wrote and edited the manuscript. YYK performed electrophysiology and Rb efflux experiments, analyzed data, prepared figures, and edited the manuscript. PZ analyzed data, prepared figures and edited the manuscript. AE designed the Rb efflux experiments, prepared figures and edited the manuscript. SLS conceived the project, performed electrophysiology experiments, wrote and edited the manuscript.

Acknowledgements

A portion of this research was supported by NIH grant U24GM129547 and performed at the Pacific Northwest Cryo-EM Center (PNCC) at Oregon Health and Science University and accessed through EMSL (grid.436923.9), a DOE Office of Science User Facility sponsored by the Office of Biological and Environmental Research, with special thanks to Dr. Nancy Meyer for help with cryoEM data collection. We acknowledge the support by the National Institutes of Health grant R01DK066485 (to SLS) and the OHSU Tartar trust foundation (to CMD). We are grateful to Zhongying Yang for help preparing adenovirus constructs and John Allen for preparing plasmids. We thank Drs. Min Woo Sung, and Bruce L. Patton for helpful discussions and Dr. Bruce L. Patton for comments on the manuscript.

References

1. Aguilar-Bryan, L. and J. Bryan, *Molecular biology of adenosine triphosphate-sensitive potassium channels.* Endocr Rev, 1999. **20**(2): p. 101-35.
2. Ashcroft, F.M., *K(ATP) channels and insulin secretion: a key role in health and disease.* Biochem Soc Trans, 2006. **34**(Pt 2): p. 243-6.

3. Nichols, C.G., *KATP channels as molecular sensors of cellular metabolism.* Nature, 2006. **440**(7083): p. 470-6.

4. Clement, J.P.t., et al., *Association and stoichiometry of K(ATP) channel subunits.* Neuron, 1997. **18**(5): p. 827-38.

5. Shyng, S. and C.G. Nichols, *Octameric stoichiometry of the KATP channel complex.* J Gen Physiol, 1997. **110**(6): p. 655-64.

6. Driggers, C.M. and S.L. Shyng, *Mechanistic insights on KATP channel regulation from cryo-EM structures.* J Gen Physiol, 2023. **155**(1).

7. Puljung, M.C., *Cryo-electron microscopy structures and progress toward a dynamic understanding of KATP channels.* J Gen Physiol, 2018. **150**(5): p. 653-669.

8. ElSheikh, A. and S.L. Shyng, *K(ATP) channel mutations in congenital hyperinsulinism: Progress and challenges towards mechanism-based therapies.* Front Endocrinol (Lausanne), 2023. **14**: p. 1161117.

9. Rosenfeld, E., A. Ganguly, and D.D. De Leon, *Congenital hyperinsulinism disorders: Genetic and clinical characteristics.* Am J Med Genet C Semin Med Genet, 2019. **181**(4): p. 682-692.

10. Pipatpolkai, T., et al., *New insights into KATP channel gene mutations and neonatal diabetes mellitus.* Nat Rev Endocrinol, 2020. **16**(7): p. 378-393.

11. Baukrowitz, T., et al., *PIP2 and PIP as determinants for ATP inhibition of KATP channels.* Science, 1998. **282**(5391): p. 1141-4.

12. Shyng, S.L. and C.G. Nichols, *Membrane phospholipid control of nucleotide sensitivity of KATP channels.* Science, 1998. **282**(5391): p. 1138-41.

13. Hibino, H., et al., *Inwardly rectifying potassium channels: their structure, function, and physiological roles.* Physiol Rev, 2010. **90**(1): p. 291-366.

14. Dickson, E.J. and B. Hille, *Understanding phosphoinositides: rare, dynamic, and essential membrane phospholipids.* Biochem J, 2019. **476**(1): p. 1-23.

15. Enkvetchakul, D., et al., *The kinetic and physical basis of K(ATP) channel gating: toward a unified molecular understanding.* Biophys J, 2000. **78**(5): p. 2334-48.

16. Hansen, S.B., X. Tao, and R. MacKinnon, *Structural basis of PIP2 activation of the classical inward rectifier K+ channel Kir2.2.* Nature, 2011. **477**(7365): p. 495-8.

17. Niu, Y., et al., *Cryo-EM analysis of PIP2 regulation in mammalian GIRK channels.* Elife, 2020. **9**.

18. Whorton, M.R. and R. MacKinnon, *Crystal structure of the mammalian GIRK2 K+ channel and gating regulation by G proteins, PIP2, and sodium.* Cell, 2011. **147**(1): p. 199-208.

19. Zhang, Y., X. Tao, and R. MacKinnon, *Correlation between structure and function in phosphatidylinositol lipid-dependent Kir2.2 gating.* Proc Natl Acad Sci U S A, 2022. **119**(12): p. e2114046119.

20. Tucker, S.J., et al., *Truncation of Kir6.2 produces ATP-sensitive K+ channels in the absence of the sulphonylurea receptor.* Nature, 1997. **387**(6629): p. 179-83.

21. Li, N., et al., *Structure of a Pancreatic ATP-Sensitive Potassium Channel.* Cell, 2017. **168**(1-2): p. 101-110 e10.

22. Martin, G.M., et al., *Cryo-EM structure of the ATP-sensitive potassium channel illuminates mechanisms of assembly and gating.* Elife, 2017. **6**.

23. Lee, K.P.K., J. Chen, and R. MacKinnon, *Molecular structure of human KATP in complex with ATP and ADP.* Elife, 2017. **6**.

24. Babenko, A.P. and J. Bryan, *Sur domains that associate with and gate KATP pores define a novel gatekeeper.* J Biol Chem, 2003. **278**(43): p. 41577-80.

25. Chan, K.W., H. Zhang, and D.E. Logothetis, *N-terminal transmembrane domain of the SUR controls trafficking and gating of Kir6 channel subunits.* EMBO J, 2003. **22**(15): p. 3833-43.

26. Martin, G.M., B.L. Patton, and S.L. Shyng, *K(ATP) channels in focus: Progress toward a structural understanding of ligand regulation.* Curr Opin Struct Biol, 2023. **79**: p. 102541.

27. Zhao, C. and R. MacKinnon, *Molecular structure of an open human KATP channel.* Proc Natl Acad Sci U S A, 2021. **118**(48).

28. Wang, M., et al., *Structural insights into the mechanism of pancreatic KATP channel regulation by nucleotides.* Nat Commun, 2022. **13**(1): p. 2770.

29. Lin, C.W., et al., *Membrane phosphoinositides control insulin secretion through their effects on ATP-sensitive K+ channel activity.* Diabetes, 2005. **54**(10): p. 2852-2858.

30. Shyng, S.L., et al., *Modulation of nucleotide sensitivity of ATP-sensitive potassium channels by phosphatidylinositol-4-phosphate 5-kinase.* Proc Natl Acad Sci U S A, 2000. **97**(2): p. 937-41.

31. Koster, J.C., et al., *ATP and sulfonylurea sensitivity of mutant ATP-sensitive K+ channels in neonatal diabetes: implications for pharmacogenomic therapy.* Diabetes, 2005. **54**(9): p. 2645-54.

32. Proks, P., et al., *Molecular basis of Kir6.2 mutations associated with neonatal diabetes or neonatal diabetes plus neurological features.* Proc Natl Acad Sci U S A, 2004. **101**(50): p. 17539-44.

33. Tammaro, P., et al., *Kir6.2 mutations causing neonatal diabetes provide new insights into Kir6.2-SUR1 interactions.* EMBO J, 2005. **24**(13): p. 2318-30.

34. Martin, G.M., et al., *Anti-diabetic drug binding site in a mammalian KATP channel revealed by Cryo-EM.* Elife, 2017. **6**.

35. Martin, G.M., et al., *Mechanism of pharmacochaperoning in a mammalian KATP channel revealed by cryo-EM.* Elife, 2019. **8**.

36. Sung, M.W., et al., *Ligand-mediated Structural Dynamics of a Mammalian Pancreatic KATP Channel.* J Mol Biol, 2022. **434**(19): p. 167789.

37. Barneda, D., et al., *How is the acyl chain composition of phosphoinositides created and does it matter?* Biochem Soc Trans, 2019. **47**(5): p. 1291-1305.

38. Rohacs, T., et al., *Specificity of activation by phosphoinositides determines lipid regulation of Kir channels.* Proc Natl Acad Sci U S A, 2003. **100**(2): p. 745-50.

39. Xu, H., et al., *Distinct histidine residues control the acid-induced activation and inhibition of the cloned K(ATP) channel.* J Biol Chem, 2001. **276**(42): p. 38690-6.

40. Wang, R., et al., *Kir6.2 channel gating by intracellular protons: subunit stoichiometry for ligand binding and channel gating.* J Membr Biol, 2006. **213**(3): p. 155-64.

41. Sung, M.W., et al., *Ligand-mediated Structural Dynamics of a Mammalian Pancreatic K(ATP) Channel.* J Mol Biol, 2022. **434**(19): p. 167789.

42. Ding, D., et al., *The Structural Basis for the Binding of Repaglinide to the Pancreatic KATP Channel.* Cell Rep, 2019. **27**(6): p. 1848-1857 e4.

43. Krissinel, E. and K. Henrick, *Inference of macromolecular assemblies from crystalline state.* J Mol Biol, 2007. **372**(3): p. 774-97.

44. Wang, M., et al., *Structural insights into the mechanism of pancreatic K(ATP) channel regulation by nucleotides.* Nat Commun, 2022. **13**(1): p. 2770.

45. Ribalet, B., S.A. John, and J.N. Weiss, *Regulation of cloned ATP-sensitive K channels by phosphorylation, MgADP, and phosphatidylinositol bisphosphate (PIP(2)): a study of channel rundown and reactivation.* J Gen Physiol, 2000. **116**(3): p. 391-410.

46. Pratt, E.B., et al., *Engineered interaction between SUR1 and Kir6.2 that enhances ATP sensitivity in KATP channels.* J Gen Physiol, 2012. **140**(2): p. 175-87.

47. Tammaro, P., P. Proks, and F.M. Ashcroft, *Functional effects of naturally occurring KCNJ11 mutations causing neonatal diabetes on cloned cardiac KATP channels.* J Physiol, 2006. **571**(Pt 1): p. 3-14.

48. Wu, J.X., et al., *Ligand binding and conformational changes of SUR1 subunit in pancreatic ATP-sensitive potassium channels.* Protein Cell, 2018. **9**(6): p. 553-567.

49. Pratt, E.B., et al., *N-terminal transmembrane domain of SUR1 controls gating of Kir6.2 by modulating channel sensitivity to PIP2.* J Gen Physiol, 2011. **137**(3): p. 299-314.

50. Wang, W., M.R. Whorton, and R. MacKinnon, *Quantitative analysis of mammalian GIRK2 channel regulation by G proteins, the signaling lipid PIP2 and Na+ in a reconstituted system.* Elife, 2014. **3**: p. e03671.

51. Pipatpolkai, T., et al., *The dynamic interplay of PIP(2) and ATP in the regulation of the K(ATP) channel.* J Physiol, 2022. **600**(20): p. 4503-4519.

52. Cukras, C.A., I. Jeliazkova, and C.G. Nichols, *The role of NH2-terminal positive charges in the activity of inward rectifier KATP channels.* J Gen Physiol, 2002. **120**(3): p. 437-46.

53. Usher, S.G., F.M. Ashcroft, and M.C. Puljung, *Nucleotide inhibition of the pancreatic ATP-sensitive K+ channel explored with patch-clamp fluorometry.* Elife, 2020. **9**.

54. Salonen, L.M., M. Ellermann, and F. Diederich, *Aromatic rings in chemical and biological recognition: energetics and structures.* Angew Chem Int Ed Engl, 2011. **50**(21): p. 4808-42.

55. Ma, J.C. and D.A. Dougherty, *The Cationminus signpi Interaction.* Chem Rev, 1997. **97**(5): p. 1303-1324.

56. De Franco, E., et al., *Update of variants identified in the pancreatic beta-cell K(ATP) channel genes KCNJ11 and ABCC8 in individuals with congenital hyperinsulinism and diabetes.* Hum Mutat, 2020. **41**(5): p. 884-905.

57. Himmel, B. and G. Nagel, *Protein kinase-independent activation of CFTR by phosphatidylinositol phosphates.* EMBO Rep, 2004. **5**(1): p. 85-90.

58. Driggers, C.M. and S.L. Shyng, *Production and purification of ATP-sensitive potassium channel particles for cryo-electron microscopy.* Methods Enzymol, 2021. **653**: p. 121-150.

59. Sung, M.W., et al., *Vascular KATP channel structural dynamics reveal regulatory mechanism by Mg-nucleotides.* Proc Natl Acad Sci U S A, 2021. **118**(44).

60. Punjani, A., et al., *cryoSPARC: algorithms for rapid unsupervised cryo-EM structure determination.* Nat Methods, 2017. **14**(3): p. 290-296.

61. Punjani, A., H. Zhang, and D.J. Fleet, *Non-uniform refinement: adaptive regularization improves single-particle cryo-EM reconstruction.* Nat Methods, 2020. **17**(12): p. 1214-1221.

62. Pettersen, E.F., et al., *UCSF ChimeraX: Structure visualization for researchers, educators, and developers.* Protein Sci, 2021. **30**(1): p. 70-82.

63. Scheres, S.H. and S. Chen, *Prevention of overfitting in cryo-EM structure determination.* Nat Methods, 2012. **9**(9): p. 853-4.

64. Gomez-Blanco, J., et al., *Hierarchical autoclassification of cryo-EM samples and macromolecular energy landscape determination.* Comput Methods Programs Biomed, 2022. **216**: p. 106673.

65. Pettersen, E.F., et al., *UCSF Chimera--a visualization system for exploratory research and analysis.* J Comput Chem, 2004. **25**(13): p. 1605-12.

66. Afonine, P.V., et al., *Real-space refinement in PHENIX for cryo-EM and crystallography.* Acta Crystallogr D Struct Biol, 2018. **74**(Pt 6): p. 531-544.

67. Emsley, P., et al., *Features and development of Coot.* Acta Crystallogr D Biol Crystallogr, 2010. **66**(Pt 4): p. 486-501.

68. Echols, N., et al., *Graphical tools for macromolecular crystallography in PHENIX.* J Appl Crystallogr, 2012. **45**(Pt 3): p. 581-586.

69. Liebschner, D., et al., *Macromolecular structure determination using X-rays, neutrons and electrons: recent developments in Phenix.* Acta Crystallogr D Struct Biol, 2019. **75**(Pt 10): p. 861-877.

70. Devaraneni, P.K., et al., *Structurally distinct ligands rescue biogenesis defects of the KATP channel complex via a converging mechanism.* J Biol Chem, 2015. **290**(12): p. 7980-91.

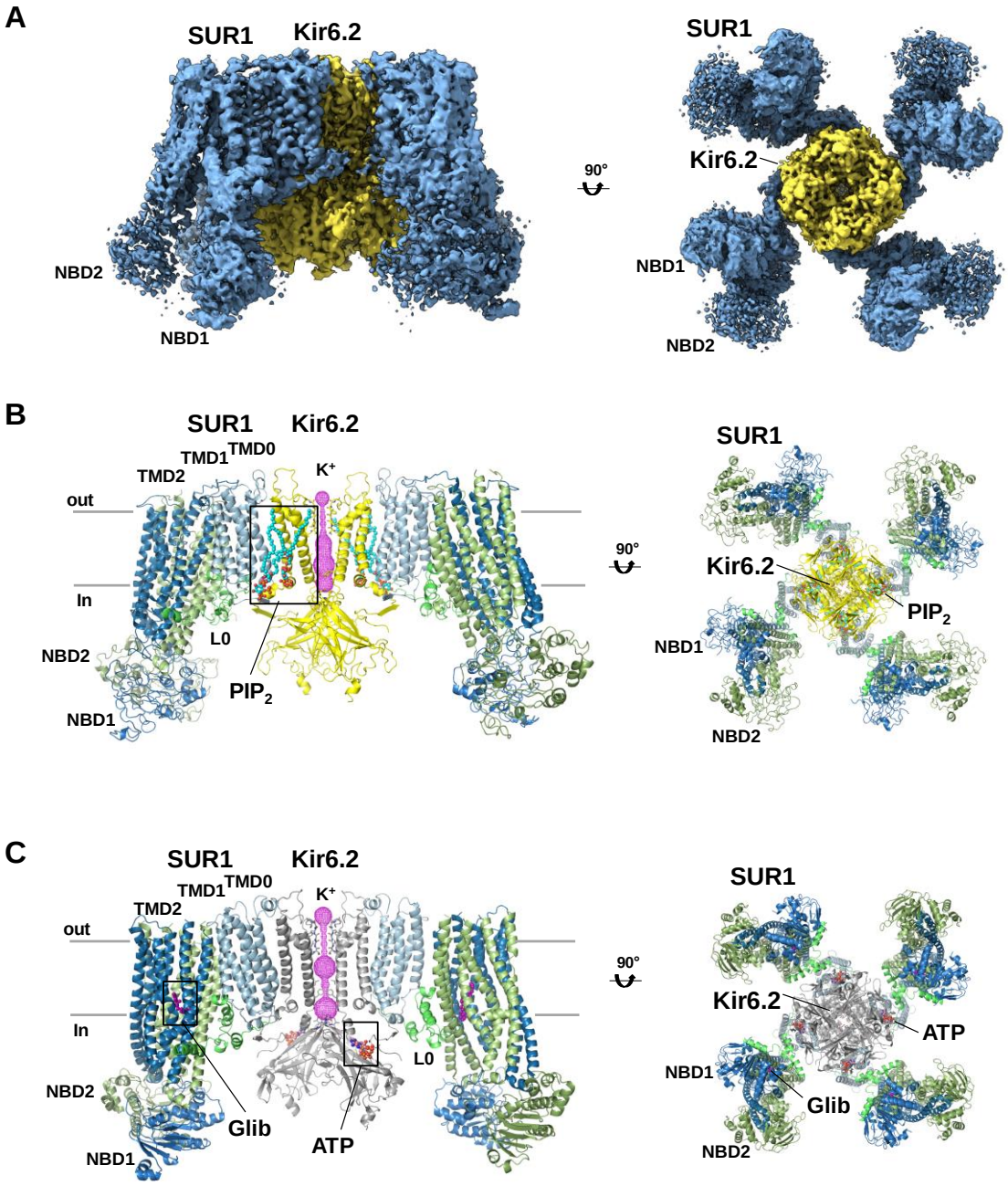

Figure 1. CryoEM structure of PIP_2-bound, open SUR1/Kir6.2^{Q52R} K_{ATP} channel. (A) The 2.9 Å cryoEM map (the micelle not shown), from C4 non-uniform refinement of 14,115 particles, shown from the side and bottom (cytoplasmic view). **(B)** Structural model of the SUR1/Kir6.2^{Q52R} K_{ATP} channel in complex with PIP_2. Only two Kir6.2 and two SUR1 subunits are shown for clarity. The potassium ion selectivity filter is shown as sticks with oxygens colored red, the K^+ conduction pathway is shown as magenta mesh and PIP_2 as sticks with cyan carbons. A view rotated 90° shown from the bottom (cytoplasmic view) displays all four Kir6.2 subunits and all four SUR1 subunits. **(C)** Structural model of a closed WT SUR1/Kir6.2 K_{ATP} channel in complex with ATP and gliblenclamide (Glib) (PDB ID 6BAA), shown for comparison and rendered similar to (B), except for the Kir6.2 subunits which are colored grey.

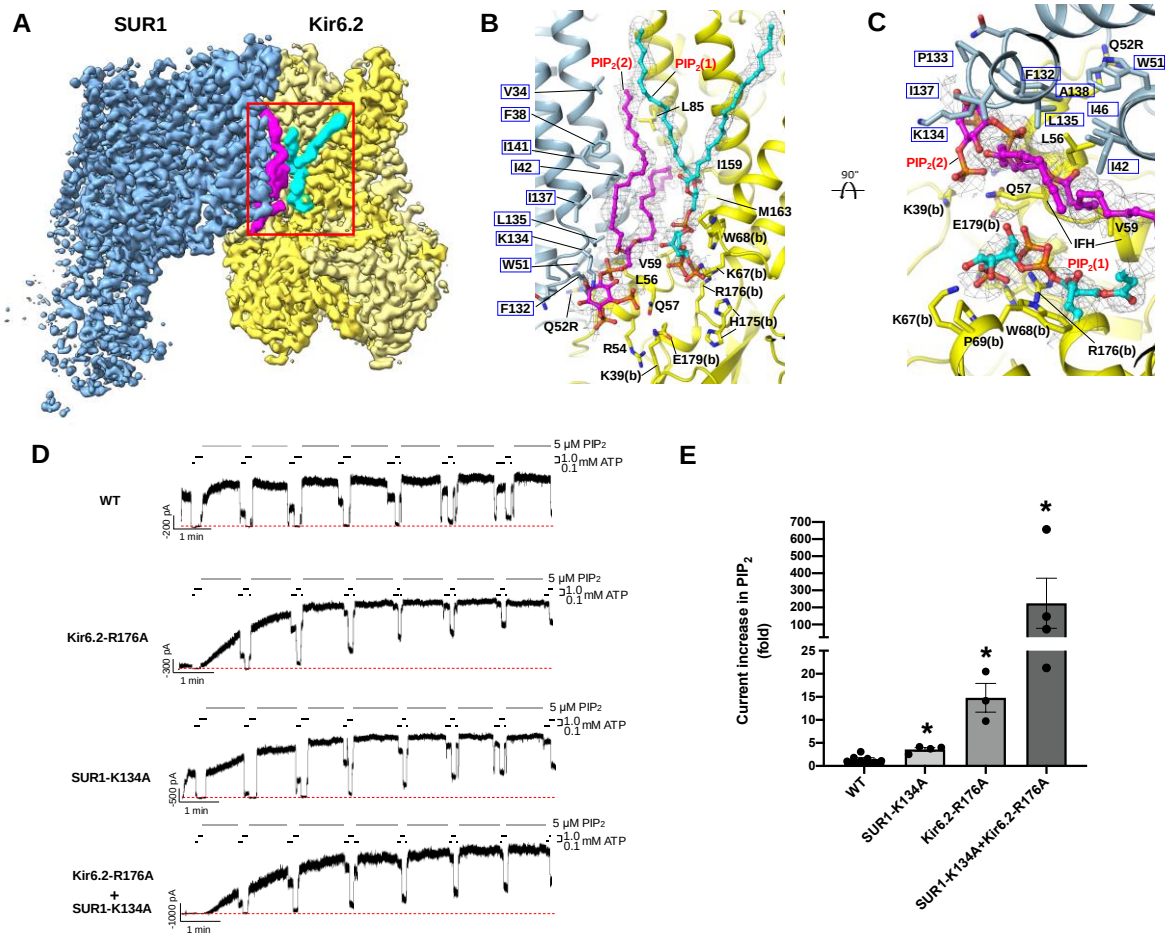

Figure 2. Two PIP_2 binding sites at the interface of Kir6.2 and SUR1. (A) CryoEM map features of two PIP_2 molecules colored in magenta and cyan (0.08V, 4.0σ contour), respectively. **(B)** Structural model of the PIP_2 binding pocket (red boxed region in (A)) viewed from the side. Residues from both Kir6.2 (adjacent subunit denoted "b") and SUR1 (blue outline) surrounding bound PIP_2 molecules are labeled. **(C)** Structural model of the PIP_2 binding pocket view from the top (extracellular side). **(D)** Representative inside-out patch-clamp recordings (-50mV, inward currents shown as upward deflections) of various channels: WT, SUR1-K134A (the second PIP_2 binding site mutation)/Kir6.2, SUR1/Kir6.2-R176A (the first PIP_2 binding site mutation), and SUR1-K134A/Kir6.2-R176A double mutant, exposed alternately in 5 μM PIP_2, 0.1 mM ATP, and 1 mM ATP as indicated by the bars above the recordings. **(E)** Group data of recordings shown in (D) showing maximum fold-increase in currents after PIP_2 exposure. Each bar represents mean ± SEM of 5-9 patches. *Statistical significance between WT and each mutant, by two-tailed Student's *t*-test, $p < 0.005$.

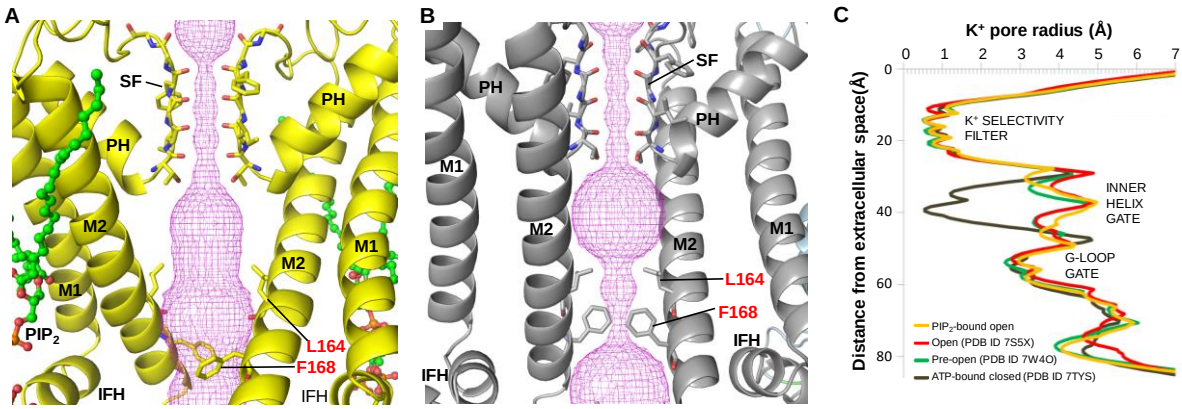

Figure 3. Comparison of the inner helix gate in the open and closed K_{ATP} channel structures. (A) Structure of Kir6.2^{Q52R} in a PIP_2-bound open state. Bound PIP_2 are shown as green and red sticks and spheres, and the side chains of inner helix gating residues L164 and F168 at the helix bundle crossing are shown as yellow sticks and labeled in red. The pore for the ion pathway (purple mesh) is constricted at the selectivity filter (SF) but open at the inner helix gate (3.3 Å). The transmembrane α-helices (M1 and M2), the interfacial α-helices (IFH) and the pore α-helices (PH) are labeled. **(B)** Kir6.2 in an ATP-bound closed state (PDB ID 6BAA) with similar labels as panel A for comparison. **(C)** Pore radii for ion conduction pathway plotted against the distance from the extracellular opening, with the location of the selectivity filter (residues 130-133), the inner helix gate (residues L164 and F168), and the G-loop gate (residues 294-297) shown. The pore radii were calculated using the program HOLE implemented in coot and viewed using a MOLE rendering in PyMOL.

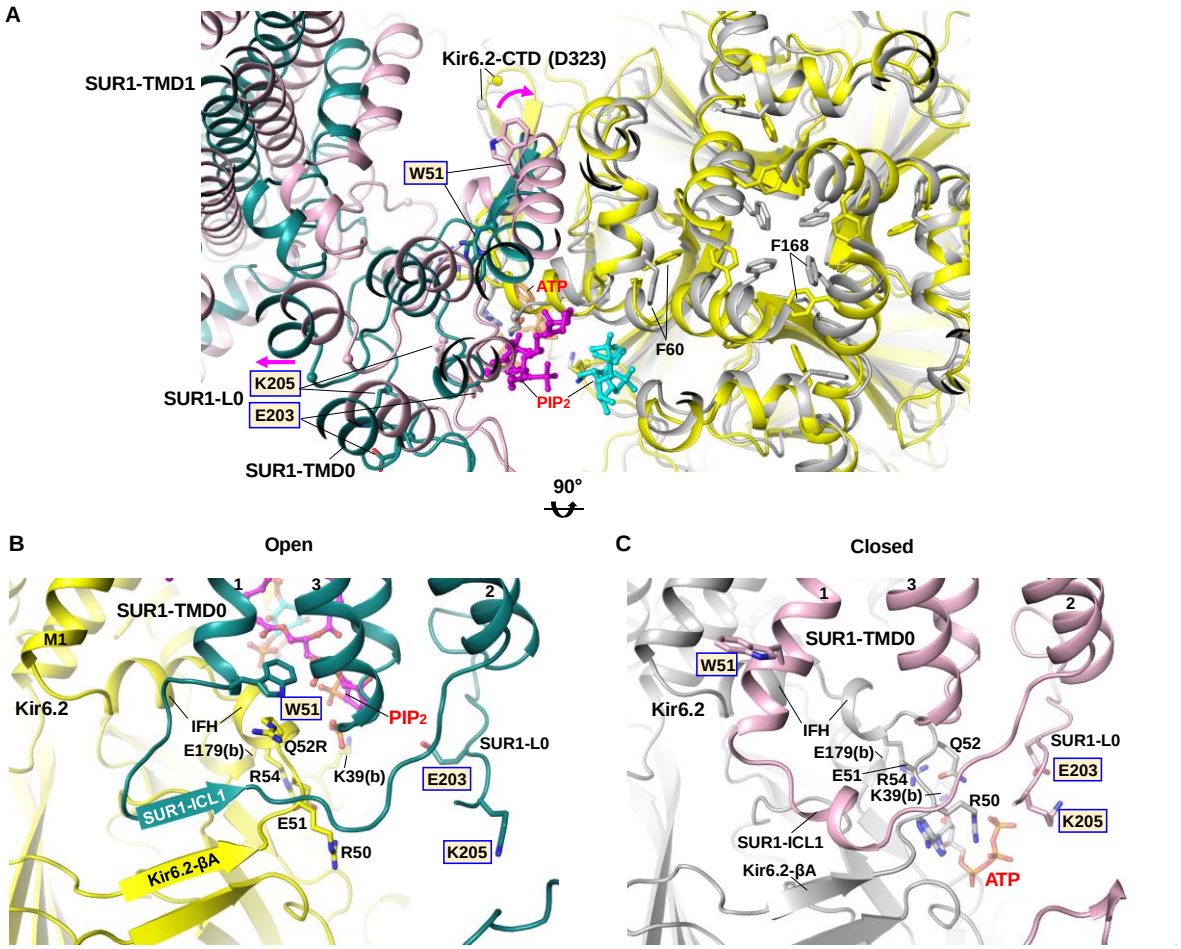

Figure 4. SUR1 and Kir6.2 cytoplasm-plasma membrane interface in open and closed K_{ATP} channel conformations. (A) An overlay of the SUR1-Kir6.2 cytoplasm-plasma membrane interface between open PIP_2 (cyan and magenta sticks)-bound SUR1/Kir6.2^{Q52R} (SUR1 in teal and Kir6.2 in yellow) K_{ATP} channel and closed ATP- (orange phosphate and grey carbon sticks) and repaglinide (out of view)-bound WT (SUR1 in pink and Kir6.2 in grey) K_{ATP} channel (PDB ID 7TYS) viewed from the extracellular side. Reorientation of side chains of the Kir6.2 inner helix gate residue F168 and M1 residue F60 in the two conformations is shown. A 6.4° clockwise rotation of the Kir6.2-CTD is indicated by the magenta curved arrow (with D323 Cα in each structure marked as spheres). Reorientation of the side chain of W51 at the bottom of TM1 of SUR1-TMD0 is evident. SUR1-L0, marked by the ATP-binding residue K205 and an adjacent residue E203, moves away from the ATP binding pocket (magenta arrow) in the open conformation. **(B)** A side view of the interface in the open conformation. SUR1-intracellular loop 1 (ICL1) forms a β-sheet with Kir6.2-βA just before the interfacial helix (IFH). Remodeling of residues involved in ATP binding and gating compared to the closed conformation in (C), including Kir6.2-R50, R54, E51 and K39(b) (from the adjacent subunit chain b) as well as SUR1-E203 and K205 in L0 are shown. Most notably, the Kir6.2 mutant residue Q52R has its side chain reoriented to interact with the side chain of SUR1-W51 which also has its side chain reoriented from the closed conformation. Color scheme same as (A). **(C)** The same side view as in (B) but of the closed conformation. In all panels, SUR1 residue labels are outlined in blue.

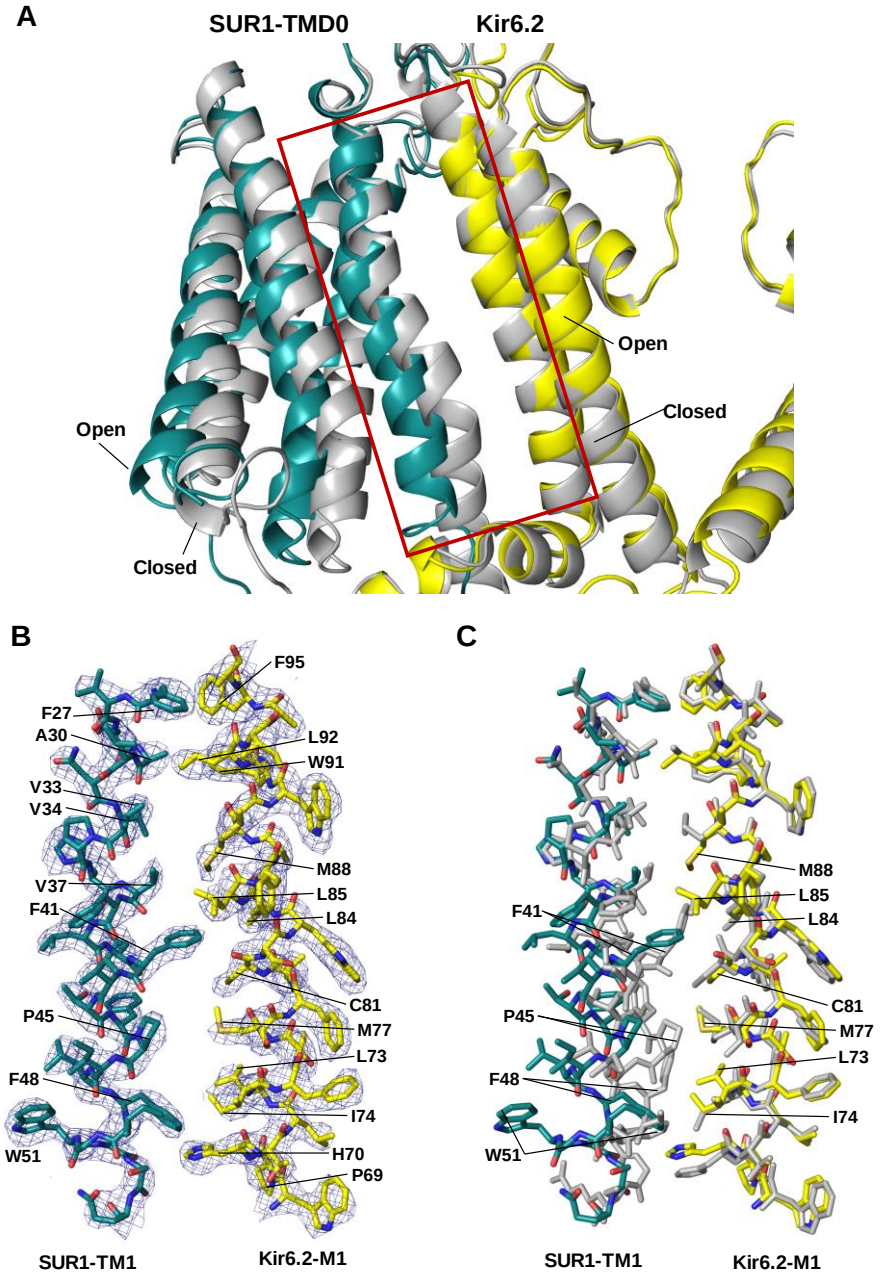

Figure 5. Structural changes between open- and closed-forms of the K_{ATP} channel at the SUR1 and Kir6.2 TM interface. (A) An overlay of the SUR1-Kir6.2 TM interface between open SUR1/Kir6.2^{Q52R} K_{ATP} channel and the closed K_{ATP} channel (PDB ID 6BAA) showing the outward movement of the cytoplasmic half of the SUR1-TMD0. In the open structure, SUR1 is shown in teal and Kir6.2 in yellow. The closed structure is shown in grey. **(B)** Close-up view of the open structure in the boxed region in (A). CryoEM map (blue mesh, 0.17V/8.5σ map contour) is superposed with the structural model. For clarity, PIP_2 is omitted. **(C)** An overlay of the open with the closed K_{ATP} channel structures in the boxed region in (A) (same color scheme) showing significant changes in residues of SUR1-TM1 at the inner leaflet half of the plasma membrane.

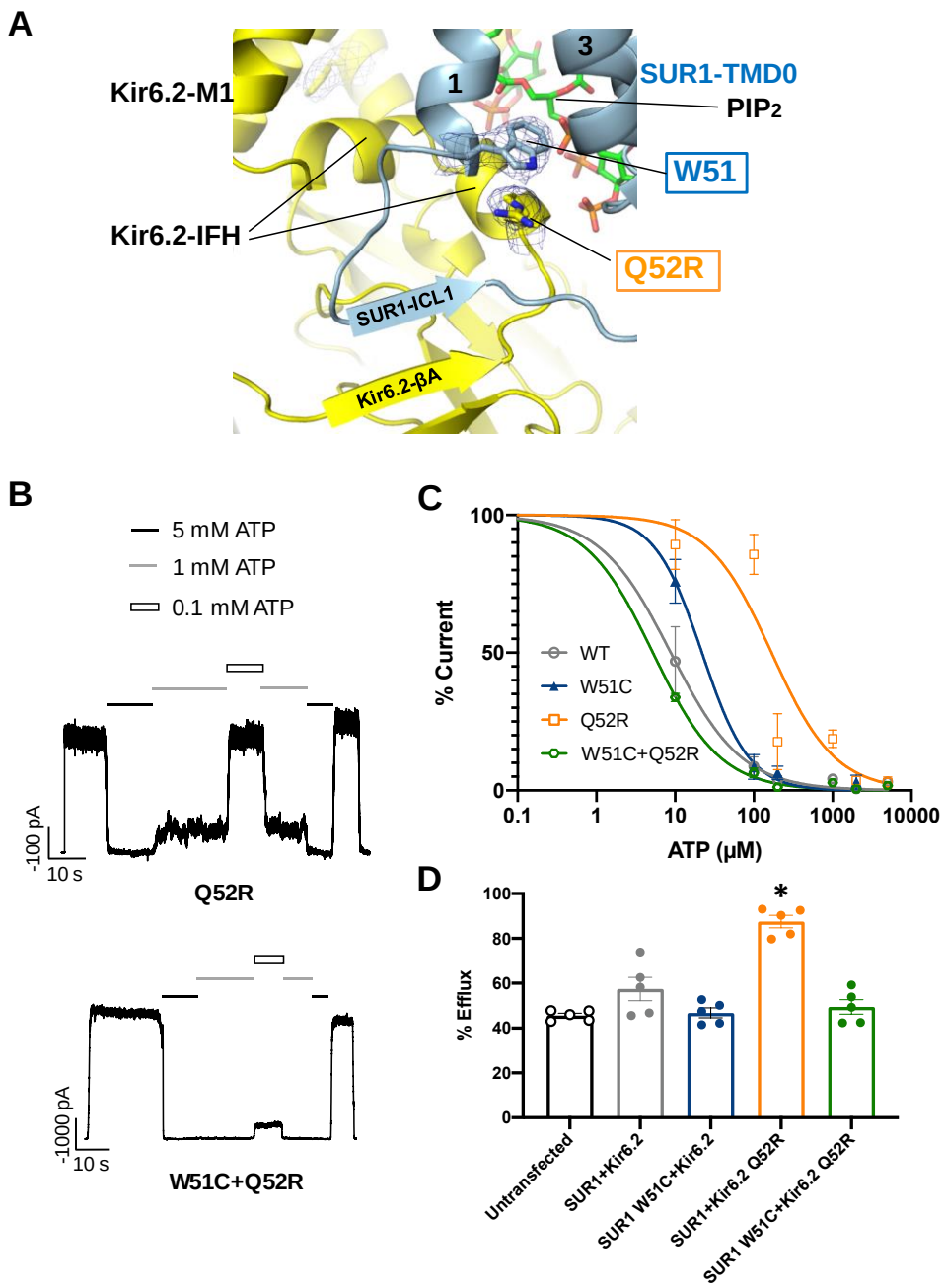

Figure 6. Kir6.2-Q52R interacts with SUR1-W51 to reduce channel sensitivity to ATP inhibition and enhance channel activity. (A) A close-up view of the interaction between Kir6.2-Q52R and SUR1-W51 with cryoEM map (blue mesh, 0.17V/8.5σ contour) superposed with the structural model. **(B)** Representative inside-out patch-clamp recordings (-50mV, inward currents shown as upward deflections) of the WT-SUR1/Kir6.2-Q52R (Q52R) channels and SUR1-W51C/Kir6.2-Q52R (W51C+Q52R) channels exposed to differing concentrations of ATP as indicated by the bars above the recordings. **(C)** ATP dose response of WT, SUR1-W51C/Kir6.2, SUR1/Kir6.2-Q52R (Q52R), and SUR1-W51C/Kir6.2-Q52R (Q52R+W51C) channels. Curves were obtained by fitting the data points (mean ± SEM of 3-5 patches) to the Hill equation (see Methods). **(D)** Rb^+ efflux of various channels expressed in COSm6 cells. Untransfected cells were included to show background efflux. Only SUR1/Kir6.2^{Q52R} channels show significant activity above WT ($p < 0.05$, n=5; one-way ANOVA with Tukey post hoc test).

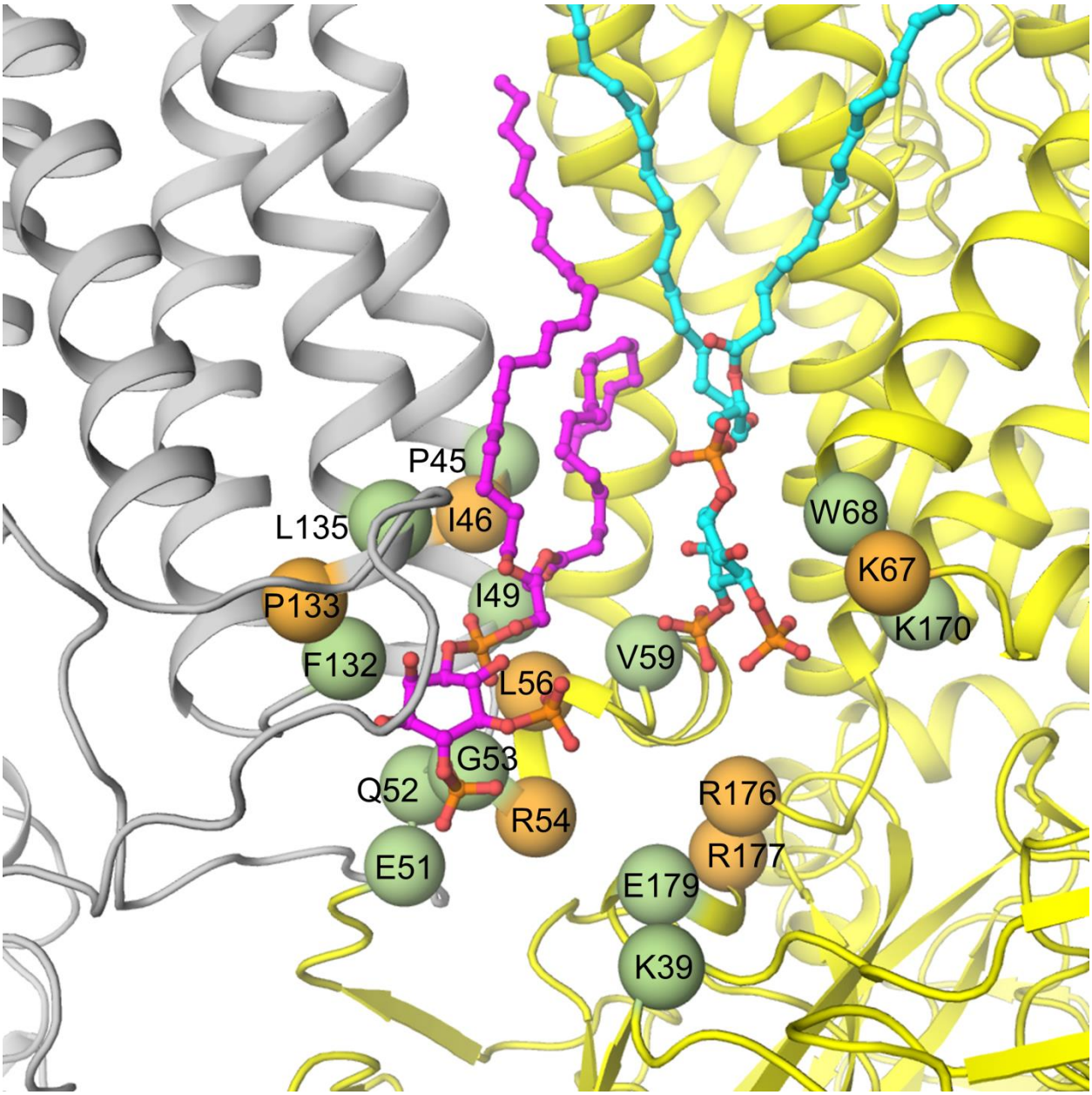

Figure 7. K_{ATP} channel disease mutations near the PIP_2 binding pocket. Residues with variants that have been reported to cause neonatal diabetes/DEND syndrome are shown as green spheres and congenital hyperinsulinism shown as orange spheres. Neonatal diabetes/DEND syndrome mutations include SUR1-P45L, I49F, F132L/V, L135P, and Kir6.2-K39R, E51A/G, Q52L/R, G53D/N/R/S/R/V, V59A/G/M, W68C/G/L/R, K170N/R/T, E179A/K. Congenital hyperinsulinism mutations include SUR1-I46T, P133R and L135V, and Kir6.2-R54C, L56G, K67D, R176H, and R177W.

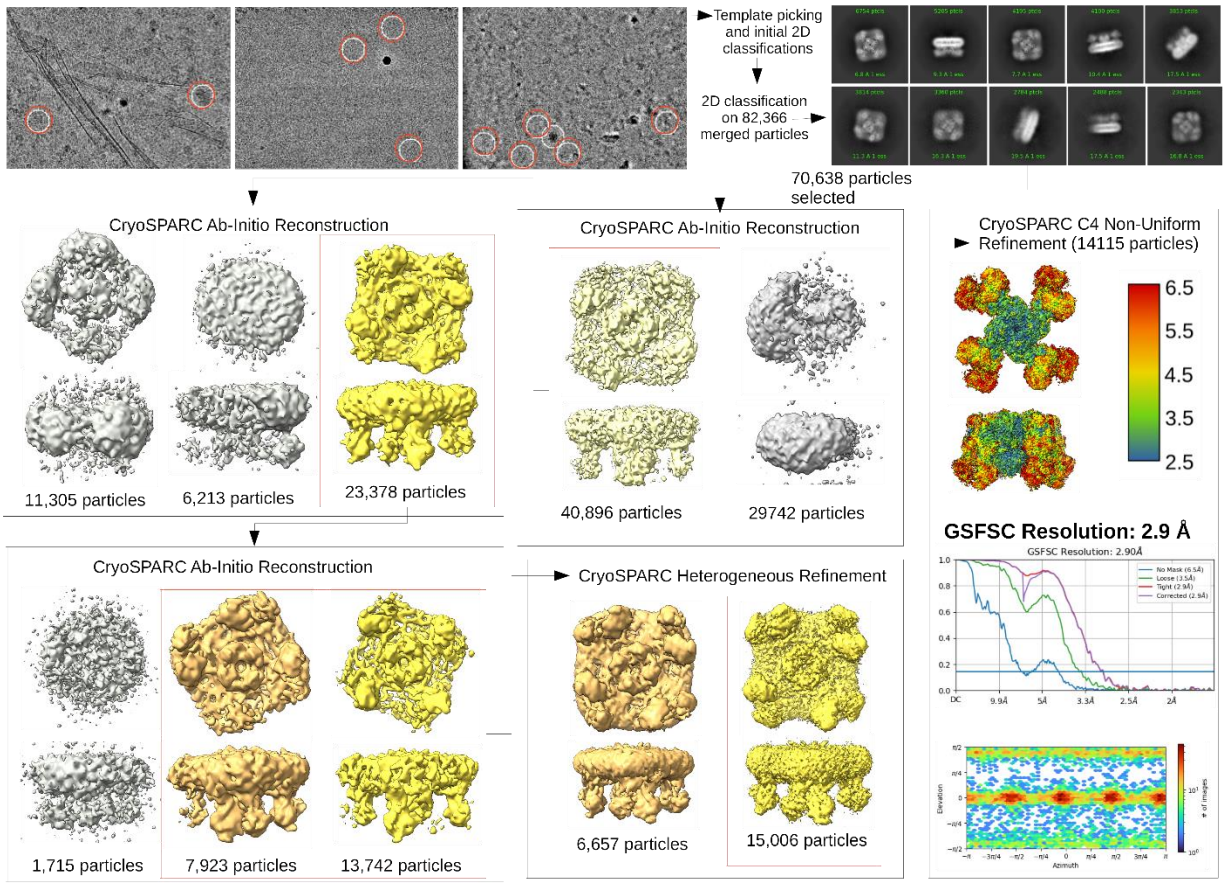

Figure S1. CryoEM data processing workflow. The total number of particles yielding the 2.9 Å C4 Non-uniform refinement reconstruction is 14,115 (FSC auto mask for GSFSC calculation).

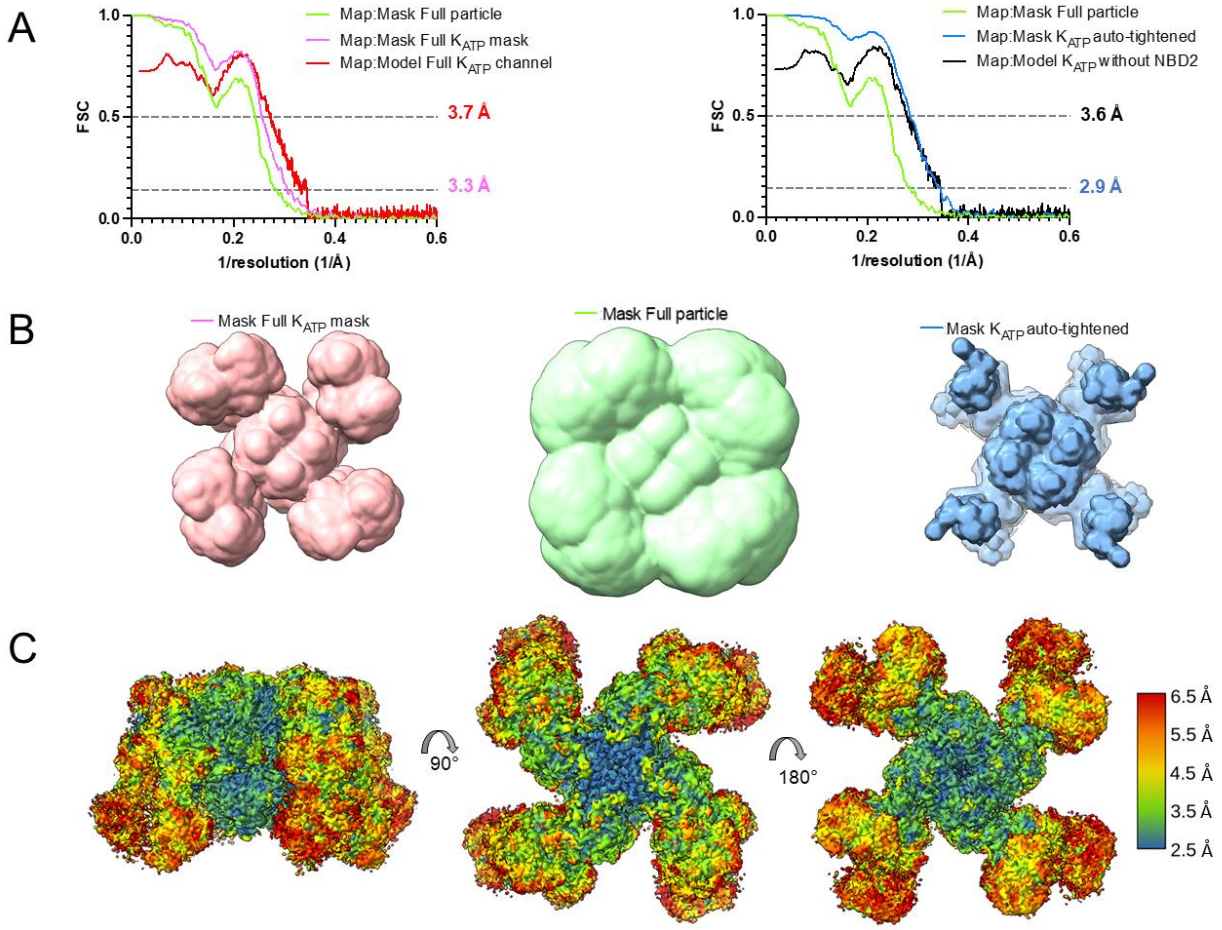

Figure S2. Fourier Shell Correlation (FSC) curves and local resolution for the C4 non-uniform reconstruction of 14,115 particles. (A) FSC curves between two independent half-maps calculated within a mask for the full particle including micelle (green), a mask for full K_{ATP} channel without the micelle (pink), and a mask created by cryoSPARC auto-mask tightening that excludes NBD2 (blue). FSC curves for model:map (unmasked) for the full K_{ATP} channel model and map (PDB ID 8TI2; EMD-41278), and for the K_{ATP} channel without NBD2 (PDB ID 8TI1). **(B)** Images of the masks used for map:map FSC calculations shown from the cytoplasmic view. **(C)** The local resolution estimate for the reconstructed map at 4 σ (0.08 V) contour, with micelle density not shown, in side view (*left*), top view (*middle*) and bottom view (*right*). No local filtering or local sharpening was used for visualization. Local resolution estimates were calculated in cryoSPARC and visualized in ChimeraX. FSC curves were calculated in PHENIX and cryoSPARC.

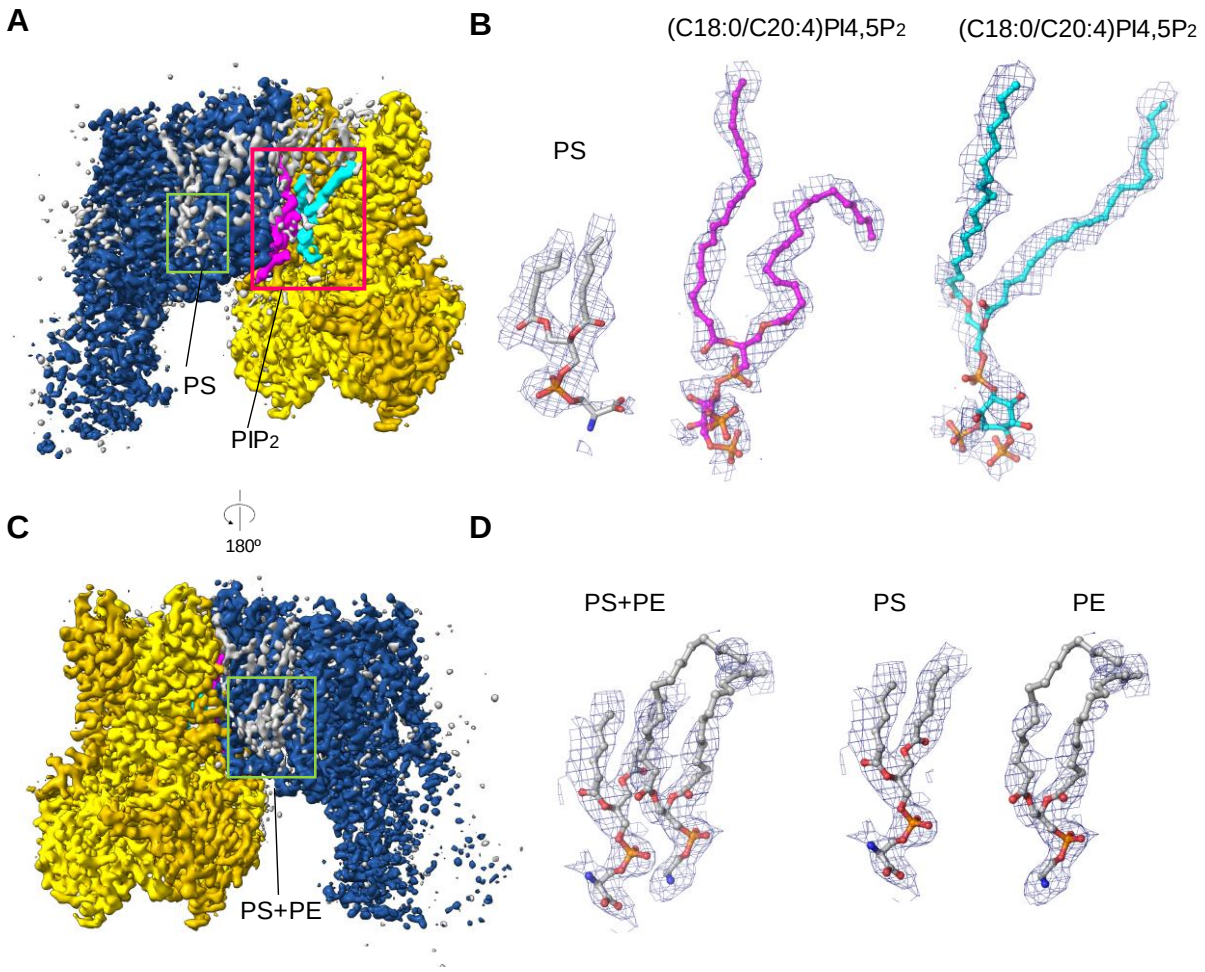

Figure S3. CryoEM lipid density fitting. (A) CryoEM map reconstructed from symmetry expansion of the ~14k particles followed by local refinement with a focused mask of Kir6.2 tetramer plus one SUR1, with density modification in Phenix and map segmentation in Chimera, shows the cryoEM densities of SUR1 and the Kir6.2 tetramer colored blue and yellow, respectively. Two PIP_2 molecules are shown in magenta and cyan, and other density including lipid density shown in grey (0.08V/4σ contour). **(B)** Isolated lipid density located between SUR1-TMD0 and SUR1-TMD1 fit with a model of phosphatidylserine (PS, grey carbons, 0.08V/4σ contour) and isolated lipid density at each of the two PIP_2 binding sites located between SUR1-TMD0 and Kir6.2 shown fit with model of the first- (cyan carbons) and second- (magenta carbons) (C18:0/C20:4) PI(4,5)P_2. **(C)** Rotation of the map 180° relative to panel A reveals other densities (grey, 0.08V/4.0σ contour) corresponding to two adjacent lipids primarily associated with the TMD0 domain. **(D)** Adjacent lipid densities can be well fit as a phosphatidylserine (PS) and phosphatidylethanolamine (PE), with the amine group of PE hydrogen bonding to the phosphate group of PS. On the right, density for each of these adjacent lipid molecules is isolated to show the fit of the lipid model into the lipid's corresponding density. These five lipid densities (20 lipids for full-channel) that are captured in the micelle are closely associated with the K_{ATP} channel and are sufficiently resolved to allow modeling.

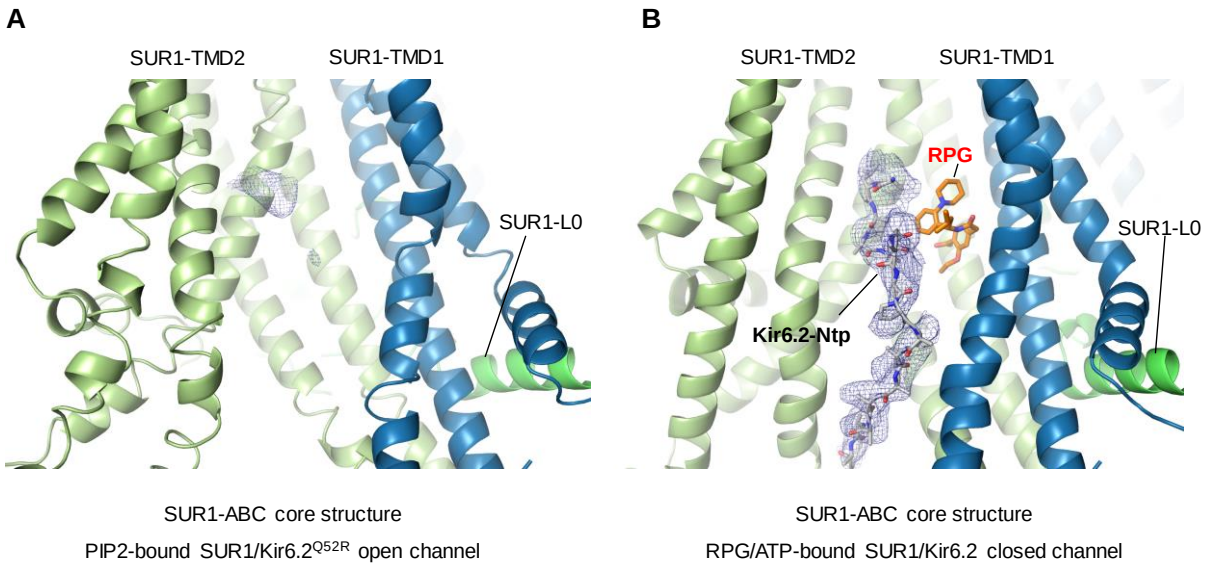

Figure S4. Comparison of the SUR1-ABC core structure in the PIP_2-bound SUR1/Kir6.2^{Q52R} open channel (A) and the repaglinide (RPG)- and ATP-bound SUR1/Kir6.2 closed channel (B). In the closed channel structure shown in (B) (EMD-26193, PDB ID 7TYS) a cryoEM density (map filtered to 6 Å and contoured to 0.5 σ) corresponding to Kir6.2-KNtp (grey stick model) next to the bound RPG is clearly visible. In contrast, in the open structure shown in (A) no comparable peptide-like cryoEM density is observed (map also filtered to 6 Å and contoured to 0.5σ), consistent with the absence of the Kir6.2-Ntp or a highly flexible Kir6.2-Ntp. Note the density protruding from SUR1-TMD2 TM helix likely corresponds to W1297 with some R1145 contribution.

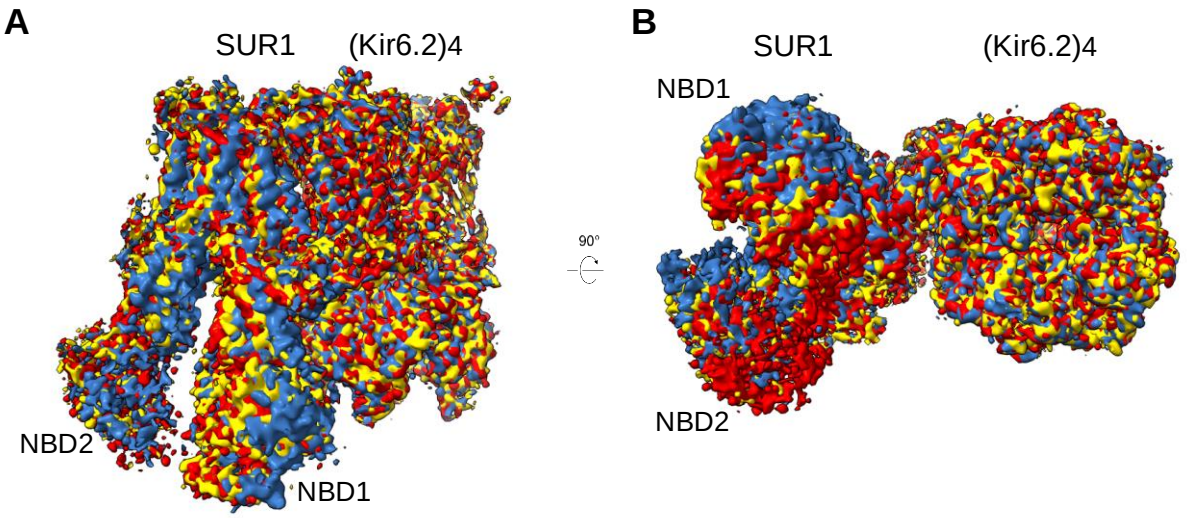

Figure S5. Conformational dynamics of the SUR1 subunit revealed by CryoSPARC 3D classification. Symmetry expansion of the 14,115 particles gave 56,460 particles, which were subjected to 3D classification with a focused mask of Kir6.2 tetramer plus one SUR1. Three unique NBD-separated SUR1 positions were resolved. **(A)** Overlay of side view maps of class 1 (3.0 Å resolution, 23,454 particles, red map), class 2 (3.3 Å resolution, 16,863 particles, yellow map) and class 3 (3.4 Å resolution, 13604 particles, blue map) reconstructed from a local non-uniform refinement with density modification in Phenix, shows the variability in SUR1 including the transmembrane regions of TMD1 and TMD2, with a common Kir6.2 tetramer position. **(B)** View from the cytoplasmic side highlights the difference in the SUR1-NBD positions, with mobility seen in both SUR1-NBD1 and SUR1-NBD2.

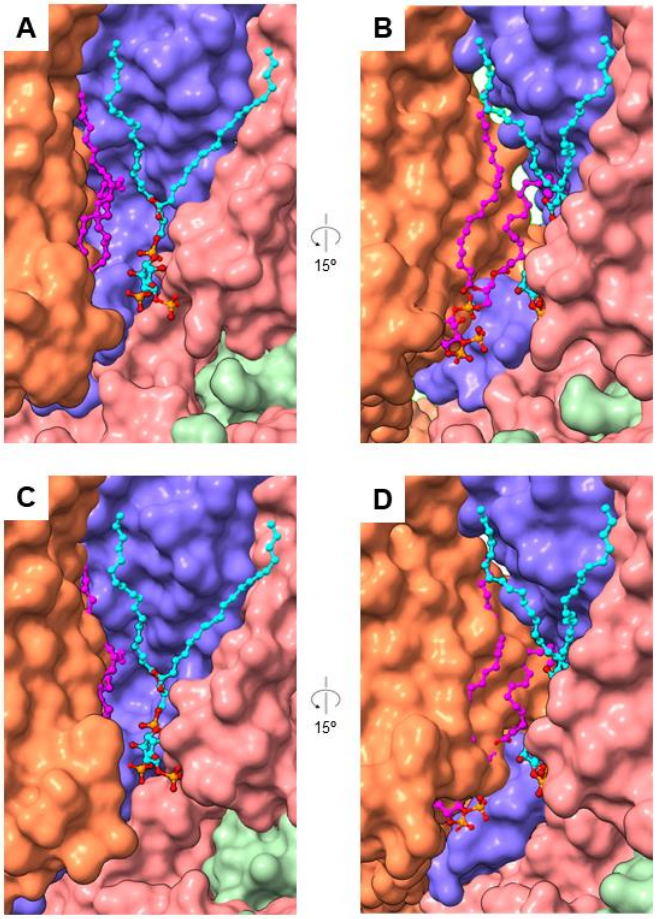

Figure S6. The K_{ATP} channel closed conformation clashes with the novel second PIP_2 molecule, but both the open and closed conformations could accommodate the conserved first PIP_2. (A,B) The open K_{ATP} channel with the conserved first PIP_2 (cyan carbons) and novel second PIP_2 (magenta carbons) shown interacting with Kir6.2 subunits (pink, green and blue surface) and the SUR1 subunit (orange surface), with the two panels rotated ~15° to show the surface of each PIP_2 site. (C,D) The closed K_{ATP} channel (PDB ID 7TYS, same surface colors as A,B) aligned with the PIP_2 molecules of the open channel shows that the closed K_{ATP} channel accommodates the conserved first PIP_2 (cyan carbons) but clashes with the novel second PIP_2 (magenta carbons).

Table S1. Model statistics of the PIP_2-bound SUR1/Kir6.2^{Q52R} structure

Data Collection		
Microscope	Titan Krios	
Voltage (kV)	300	
Camera	Gatan K3	
Camera mode	Super-resolution	
Defocus range (μm)	-1.0 ~ -2.5	
Movies	5241	
Frames/movie	78	
Exposure time (s)	2.2	
Frame rate (/s)	35	
Magnified pixel size (Å)*	0.826	
Total dose (e^-/Å^2)	~55	
Reconstruction		
Software	Cryosparc 4.2.1	Cryosparc 4.2.1
Symmetry	C4	C4
Mask	Full K_{ATP}	autoFSC tightened
Particles refined	14,115	14,115
Resolution (masked)	3.3 Å	2.9 Å
Refinement Statistics		
PDB ID[1]	8TI2	8TI1
EMDataResource	EMD-41278	EMD-41277
Atoms	50210	45034
Protein residues	6896	5848
Map CC (masked)	0.80	0.81
FSC model (0.143, 0.5)	3.0, 3.7	2.9, 3.6
Clash score	7.72	7.79
Molprobity score	2.14	2.18
Cβ deviations	0	0
Rotamer outliers (%)	3.45	3.63
ADP (mean protein)	166.3	175.5
ADP (mean ligands)	132.78	152.57
Ramachandran		
Outliers	0.23	0.22
Allowed	4.17	4.56
Favored	95.6	95.22
Bonds (RMSD)		
Length (Å)	0.003	0.003
Bond angles	0.663	0.675

[1]PDB ID 8TI2/EMD-41278 contains the full channel and full K_{ATP} mask; PDB ID 8TI1/EMD-41277 has the flexible NBD2 (residue 1317 to C-terminus) removed and the auto-FSC tightened mask.
*Super-resolution pixel size 0.4130 Å

Movie 1 Open-closed transition side view
Movie 2 Open-closed transition pore closure extracellular view